Multi-proxy record of orbital-scale changes in climate and sedimentation during the Weissert Event in the Valanginian Bersek Marl Formation (Gerecse Mts., Hungary)

Dávid Bajnai[1,2,*], József Pálfy[1,3], Mathieu Martinez[4,5], Gregory D. Price[6], Anita Nyerges[1,3], István Főzy[7]

[1] Department of Physical and Applied Geology, Eötvös Loránd University, Pázmány Péter sétány 1/C, 1117, Budapest, Hungary

[2] Institut für Geowissenschaften, J. W. Goethe-Universität, Altenhöferallee 1, 60438, Frankfurt am Main, Germany

[3] MTA-MTM-ELTE Research Group for Paleontology, POB 137, H-1431, Budapest, Hungary

[4] UMR CNRS/UPPA/Total 5150 Laboratoire des Fluides Complexes et leurs Réservoirs (LFC-R), Université de Pau et des Pays de L'Adour, BP 1155, 64013 Pau CEDEX, France

[5] MARUM – Center for Marine Environmental Sciences, Universität Bremen, Leobener Str., 28359, Bremen, Germany

[6] School of Geography, Earth & Environmental Sciences, Plymouth University, Drake Circus, PL4 8AA, Plymouth, United Kingdom

[7] Department of Palaeontology and Geology, Hungarian Natural History Museum, POB 137, 1431, Budapest, Hungary

[*] Corresponding author: david.bajnai@em.uni-frankfurt.de

Abstract

The Valanginian positive carbon isotope excursion and associated environmental changes, known as the Weissert Event, is the first in the series of Cretaceous Earth system perturbations. Here, we develop a multiproxy cyclostratigraphy from a 31.2-m-thick Upper Valanginian to lowermost Hauterivian section of the Bersek Marl Formation in Gerecse Mountains, Hungary, comprising alternating marlstone layers of varying clay and carbonate content. The bulk carbonate $\delta^{13}C$ signal shows sustained, elevated values (up to 2.7‰) up to 19.2 m, followed by a decreasing trend upsection. Together with biostratigraphic data, this suggests that the lower part of the section was deposited during the plateau phase of the Valanginian Weissert Event. Spectral analyses of the multiproxy dataset, including magnetic susceptibility measurements and gamma-ray spectroscopy on the lower part of the section led to the identification of precession, obliquity, long and short eccentricity signals. A mean sedimentation rate of 14 m/Myr was calculated based on astronomical tuning. The cyclicity in the proxy signals reflects dilution cycles by detrital inputs in the basin, which supports the idea that orbitally-forced humid-arid cycles controlled the pelagic alternating sedimentation during the Early Cretaceous throughout the Tethyan area.

1. Introduction

The Cretaceous period is well known for oceanic anoxic events (OAEs) and carbon isotope excursions (CIEs), which have been linked to the volcanism of large igneous provinces (Erba, 2004; Jenkyns, 2010). The OAEs are episodes of increased organic carbon burial in sediments driven primarily by climate warming (Schlanger and Jenkyns, 1976). The CIEs often accompany the OAEs, but they may also occur independently, with no correlated organic-rich deposits (Westermann et al., 2010; Föllmi, 2012).

The Late Valanginian Weissert Event is the first positive CIE of the Cretaceous (Weissert et al., 1998; Erba et al., 2004; Weissert and Erba, 2004; Föllmi, 2012). As organic-rich deposits are not a characteristic of this carbon isotope excursion, it is best described as a stand-alone CIE rather than an OAE (Westermann et al., 2010; Kujau et al., 2012). The Weissert Event is notably associated with a widely distributed decline in carbonate production in neritic regions (Weissert et al., 1998; Föllmi et al., 2006), increases in atmospheric pCO_2 (Morales, 2013), more humid climate conditions and intensified continental weathering (Duchamp-Alphonse et al., 2011; Kujau et al., 2013; Charbonnier et al., 2016), increases in nutrient availability in marine environments (Duchamp-Alphonse et al., 2007, 2014; Mattioli et al., 2014), and major turnover events in marine faunas (Reboulet and Atrops, 1997; Melinte and Mutterlose, 2001; Gréselle et al., 2011; Barbarin et al., 2012). Numerous studies have shown the global extent of the CIE which was first observed in deep-sea sediment cores from the Southeastern Gulf of Mexico (Cotillon and Rio, 1984), then subsequently observed in Italy (Lini et al., 1992; Channell et al., 1993; Sprovieri et al., 2006; Bersezio et al., 2002; Erba et al., 2004; Amodio et al., 2008;), in the Vocontian Trough in Southern France (Hennig et al., 1999;

van de Schootbrugge et al., 2000; Duchamp-Alphonse et al., 2007; Gréselle et al., 2011; Charbonnier et al., 2013), in the Polish Basin (Morales et al., 2015), in the Southern Carpathians in Romania (Barbu and Melinte-Dobrinescu, 2008; Grădinaru et al., 2016), in Greenland (Möller et al., 2015), in the Neuquén Basin in Argentina (Aguirre-Urreta el al., 2008), in Northeastern Mexico (Adatte et al., 2001), in Western Siberia (Price and Mutterlose, 2004), and in various deep-sea sediment cores (Katz et al., 2005; Tremolada et al., 2006; Littler et al., 2011). Continental records for the Weissert Event are also known from the Crimea and Russia (Gröcke et al., 2005; Nunn et al., 2010). In Hungary, the CIE has been documented in the Hárskút section in the Bakony Mountains (Főzy et al., 2010), where the bulk rock $\delta^{13}C$ curve reported in Főzy et al. (2010) on Biancone-type carbonates shows a positive shift that is characterised by a sharp rise and a possibly suppressed plateau phase due to sedimentary condensation.

The age of the Weissert Event and its relationship to the magmatism of a large igneous province has been subject to debate (Erba, 2004; Erba et al., 2004; Sprovieri et al., 2006; Jenkyns, 2010; Thiede and Vasconcelos, 2010; Martinez et al., 2013), in part due to significant uncertainties in the calibrated age of the Early Cretaceous stage boundaries (Hinnov and Ogg, 2007; Ogg et al., 2016). A recently obtained U-Pb age of a mid-Hauterivian tuff layer in the Neuquén Basin, Argentina (Aguirre-Urreta et al., 2015), anchored the astrochronology of the Valanginian-Hauterivian stages (Martinez et al., 2013, 2015) and led to a revision of the age of onset of the Weissert Event, now dated at 135.22 ± 1.0 Ma. This age is undistinguishable from the most precise ages calculated for the flood-basalt activity of the Paraná-Etendeka large igneous province (Thiede and Vasconcelos, 2010; Janasi et al., 2011), suggesting a link between the two events (Martinez et al., 2015).

This study focuses on the Bersek Marl Formation in Hungary that has an almost 150-year-old history of research. It was first described by Hantken (1868), who assigned an Early Cretaceous age to the marlstones of the Gerecse Mountains. Ninety years later, Fülöp (1958) provided a thorough bio- and lithostratigraphic description of these deposits. Recently, a more detailed integrated biostratigraphy for the Bersek Quarry, established by Főzy (1995), Főzy and Fogarasi (2002), and Főzy and Janssen (2009), determined a Valanginian–Hauterivian age for the upper part of the formation. The first estimate of the average sedimentation rate of the Bersek Marl Formation is based on the assessed thickness of the formation and the estimated duration of deposition based on ammonoid stratigraphy (Fogarasi, 1995b). Given an assumed average sedimentation rate of 10 m/Myr, Fogarasi (1995b) posited that the deposition of marlstone-limestone couplets in the uppermost part of the Bersek Marl Formation and the lowermost part of the overlying Lábatlan Sandstone Formation were controlled by precession cycles.

Here, the sedimentary record of the Weissert Event is investigated at the Bersek Marl Formation to produce the first record of this Early Cretaceous CIE at this locality and within this basin. The first objective was to compile a $\delta^{13}C$ record for the upper part of the Bersek Marl Formation in order to identify whether the Weissert Event is entirely or partially recorded within this section. The second objective was to accurately estimate the sedimentary deposition rate by integrating cyclostratigraphic analysis on bulk rock $\delta^{13}C$, magnetic susceptibility, and gamma-ray spectroscopy measurements. New calcareous nannoplankton and ammonoid biostratigraphic analyses were also conducted to improve the age constraint.

2. Geological setting

2.1. Tectonic and stratigraphic framework

The studied outcrop is situated in one of the abandoned yards of the Bersek Quarry, close to the village of Lábatlan within the Gerecse Mountains (Fig. 1A-B). The GPS coordinates of the studied section are: 47.72145°N and 18.52630°E. The Gerecse Mountains form part of the Transdanubian Range, which in turn belongs the ALCAPA Terrane. During the Alpine orogeny, the Transdanubian Range was interlinked with the geological formations that now form part of the Southern Alps and the Northern Calcareous Alps (Fig. 1C). The Jurassic and Cretaceous strata of the Gerecse Mountains were deposited during the evolution of a Neotethys sub-basin, starting in the Late Triassic. The Late Jurassic pelagic carbonate sedimentation changed in the Berriasian, when the thrust front advanced towards the foreland, and clastic input became the dominant factor. This change marks the formation boundary between the Szentivánhegy Limestone Formation and the overlying Bersek Marl Formation. The clastic input further increased in the Barremian sediments, as inferred from a change in lithology from marlstone to sandstone, marking the base of the Lábatlan Sandstone Formation (Főzy, 2013).

The 31.2-m thick section studied lies entirely within the Bersek Marl Formation. The base of the studied section starts at the bottom of the quarry face in this yard and the underlying strata could subsequently not be sampled. This prevented the unambiguous correlation with other quarry yards that expose deeper strata. As a hiatus separates the top of the Bersek Marl Formation and the base of the overlying Lábatlan Sandstone Formation, we decided to limit the top of the studied interval at the top of the

Bersek Marl Formation (Fig. 1D). The section studied comprises marlstone layers with fluctuating carbonate content, limestone beds, and sporadic, thin sandstone intercalations. The colour of the marlstone transitions from grey to purple at 27.8 m, dividing the section into two informal units, which we will henceforth refer to as the "grey marlstone" and the "purple marlstone". In the "grey marlstone" unit of the Bersek Marl Formation, the bed thicknesses range from a few centimetres to a few decimetres, but the lithological contrast between beds is low, making challenging to recognise the bed boundaries in the field. The bedding of the "purple marlstone" is more apparent due to the higher lithological contrast. The bed thicknesses in this unit are around 0.2–0.3 m. Centimetre-thick green turbidite beds, synsedimentary faults and slumps only occur in the "grey marlstone". Throughout the Bersek Quarry, the base of the overlying Lábatlan Sandstone Formation is marked by a few metre-thick, green sandstone beds with an erosive base, that serve as a stratigraphical marker (hereafter referred to as the "green marker bed"). A detailed stratigraphical column is provided as supplementary material.

To date, three different stratigraphic sections have been logged and studied in detail at the Bersek Quarry (Fig. 1B). The cephalopod specimens and sediment samples, used for the studies by Főzy and Fogarasi (2002), Főzy and Janssen (2009), and Price et al. (2011), were collected from Section III of Fig. 1B by a team led by J. Fülöp between 1963–65. The section studied by Főzy (1995), referred to as Section II in Fig. 1B, lies ~150 m eastwards from Section III, in a different quarry yard. Fogarasi (1995b) investigated sections practically identical to Section II and Section III. The section studied in this paper is labelled as Section I in Fig. 1B, and is located adjacent to Section II, in the same quarry yard but in a newly sampled segment of the quarry face.

Ammonoid and calcareous nannoplankton biostratigraphy have been previously developed for the uppermost strata of the Bersek Marl Formation and the lowermost part of the succeeding Lábatlan Sandstone Formation (Főzy, 1995; Főzy and Fogarasi, 2002; Főzy and Janssen, 2009). The rich cephalopod fauna of the “purple marlstone” and the Lábatlan Sandstone Formation allows the recognition of Mediterranean ammonoid zones, whilst macrofossils are scarcer in the underlying “grey marlstone”. The youngest strata of the Lábatlan Sandstone Formation, immediately overlying the thick “green marker bed”, are earliest Barremian in age (Főzy, 1995; Főzy and Fogarasi, 2002; Főzy and Janssen, 2009). In Section III, the uppermost boundary of the oldest recognised ammonoid zone, the Valanginian *Varlheideites peregrinus* Zone, is detected approximately 12 m below the “green marker bed”. In the same section the youngest recognised ammonoid zones below the “green marker bed” are the Upper Hauterivian *Pseudothurmannia ohmi* and *Balearites baelaris* Zones. The calcareous nannoplankton assemblages of the same collection led to the recognition of the NK3/NC4 and possibly of the NC4/NC5 Zone boundaries below the base of the Lábatlan Sandstone Formation (Főzy and Fogarasi, 2002; Főzy and Janssen, 2009). In Section II, studied by Főzy (1995), the characteristic Hauterivian ammonoid fauna is not present, suggesting a Late Valanginian–Early Hauterivian age for the uppermost strata of this section, directly under the base of the “green marker bed”.

The oldest strata of the Bersek Marl Formation belong to the Felsővadács Breccia Member. The oldest marlstone layers overlaying this unit are posited to be latest Barremian/earliest Valanginian in age, based on ammonite (Vigh, 1984) and nannoplankton (Fogarasi, 2001) biostratigraphy. These strata do not crop out at the Bersek Quarry, but are visible in other sections.

2.2. Palaeogeographic setting

Interpretation of the sedimentary environment of the Bersek Marl Formation has been controversial. It has been successively regarded as a shallow marine deposit (Fülöp, 1958), flysch (Császár and Haas, 1984), a bathial slope deposit (Kázmér, 1987), or as part of a submarine fan sequence (Sztanó, 1990). Fogarasi (1995a) noted that the total thickness and the sedimentation rate of the marlstone is smaller than would be expected for a submarine fan deposit and instead suggested a pelitic slope environment. According to the most recent study of Fodor et al. (2013), the Bersek Marl Formation was deposited on a forebulge, a slope facing the foreland basin, on the opposite side of the orogenic arc. It has been suggested that the difference in lithology between the "grey marlstone" and the "purple marlstone" is controlled by the basin evolution, where the deposition of "purple marlstone" could reflect an interval of subdued tectonic activity in an otherwise actively forming flexural basin (Fodor et al., 2013). The colour of the "grey marlstone" and the occurrence of small, charred plant fragments suggests suboxic bottom waters, while the reddish colour of the "purple marlstone" and the *Zoophycos*-type trace fossils could imply a transition to a more oxygenated environment (Fodor et al., 2013). Petrographic studies of Császár and Árgyelán (1994) and Árgyelán (1995) identified the source of distinctive heavy minerals in the turbidite beds as the suture zone of the Neotethys. Coeval sandstone beds, in the corresponding units in the Northern Calcareous Alps, the Schrambach and the Rossfeld Formations, have similar compositions (von Eynatten and Gaupp, 1999, Krische et al., 2013).

3. Material and methods

Fieldwork was carried out between April 2014 and August 2015, when the continuous 31.2-m thick Section I of Fig. 1B was measured and logged at the Bersek Quarry. A total of 241 bulk rock samples were collected with a uniform 0.1-m spacing in the lower 16.8 m (169 samples) and with a 0.2-m spacing in the upper 14.4 m (72 samples). The samples were cut with a diamond saw blade with low revolution speed, washed with tap water to remove the weathered surfaces, and split into ~15 g subsamples that were later processed for analyses. To avoid metallic contamination that could bias the magnetic susceptibility measurements, the sample collection was done by hand, and the samples were stored in plastic bags. Bulk rock samples are deposited in the Department of Palaeontology and Geology of the Hungarian Natural History Museum, Budapest, under inventory numbers INV 2016.215.1-241.

3.1. Stable isotope analyses

The bulk rock carbonate carbon and oxygen stable isotope analyses were performed at the University of Plymouth, on a GV Instruments IsoPrime IRMS using a Gilson 222XL autosampler. For the measurements, ~0.5 mg powder was drilled from each of the 241 bulk rock samples. Isotope ratios are reported in δ values relative to the Vienna Pee Dee belemnite (VPDB) standard. For the instrument calibration, the NBS-19, the IAEA-CO-8, and the IAEA-CO-9 standards were used. Upon replicate analyses, the standard deviation was calculated as 0.2‰ for $\delta^{13}C$ and 0.3‰ for $\delta^{18}O$.

3.2. Magnetic susceptibility measurements

The magnetic susceptibility (MS) measurements were conducted at the Université de Pau et des Pays de l'Adour on an Agico Kappabridge MFK1-FA type instrument, with a 976 Hz 200 A/m field strength. A set of 169 samples, from the bottom 16.8 m of the section, was analysed. Each sample was measured in triplicate to assess the reproducibility of the measurements. The results are given in m^3/kg (mass susceptibility). The standard deviation of the measurements is $8x10^{-3}$ m^3/kg.

3.3. Gamma-ray spectroscopy

The gamma-ray spectroscopy (GRS) measurements were conducted in the field using a hand-held Georadis RS-125 gamma-ray spectrometer. The instrument was fitted with a 103 cm^3 Na(Ti) scintillation detector with a 0.06 m diameter detector head. The lower 16.8 m of the section were analysed, except for the lowermost three sampling spots that were covered with soil. The measurements were done on the same spots where the bulk rock samples were collected from, and each spot was analysed three times for a measurement time of 120 seconds. The total ^{40}K, ^{238}U, and ^{232}Th content of the rocks are reported in uranium-equivalent ppm. The standard deviation was derived from 26 test measurements on one single spot, and it was calculated as 0.9 Ue ppm.

3.4. Time series analyses for cyclostratigraphy

Cyclostratigraphic analyses were made on bulk carbonate $\delta^{13}C$, magnetic susceptibility, and gamma-ray spectroscopy signals. Prior to spectral analysis, the raw data series were linearly interpolated every 0.1 m and long-term trends were removed. The detrending procedures applied here aim at reducing the power of the lowest frequencies towards zero whilst maintaining the powers of higher frequencies. The trends were removed from the $\delta^{13}C$, the MS, and the GRS data series by subtracting a 3rd-order polynomial regression, a 5th-order polynomial regression, and a linear regression, respectively.

The spectrum of the whole series was calculated using the multitaper method applied with three 2π-tapers (2π-MTM; Thomson, 1982, 1990). Confidence levels were calculated using robust red-noise modelling, modified according to Tukey's end-point rule (Tukey, 1977; Mann and Lees 1996; Meyers, 2014). In addition to the power spectra, two evolutive spectrograms were generated per dataset using Time–Frequency Fast Fourier Transform (T–F FFT). Firstly, for longer periodicities, an 8-m sliding window and a 0.1-m window step were applied to the complete detrended series. Secondly, for shorter periodicities, a 4-m sliding window and a 0.1-m window step were applied after a second low-pass filter was subtracted from the detrended series to exclude low-frequency, high-power cyclicities. The power spectra and the evolutive spectra are then interpreted together. Variations in the sedimentation rate can result in one Milankovitch-cycle being expressed over several frequencies on the 2π-MTM spectra of the sedimentary series (e.g., Weedon, 2003; Martinez et al., 2016). Changes in the sedimentation rate can be recognised in the evolutive spectra by the deviation of the spectral bands, assigned to the cyclicity in question (Martinez et al., 2015). To isolate certain frequencies from the rest of the series, Taner band-pass filters were applied (Taner, 2003; Meyers, 2014).

3.5. Calcareous nannoplankton

Study of the calcareous nannoplankton assemblages were not intended to be comprehensive and were therefore restricted to 12 samples. Successive highly calcareous and highly clay-rich marlstones from both the “grey marlstone” (samples BQ53–BQ56) and the “purple marlstone” (samples BB48–BB51) were targeted, which corresponded with alternating cycles of peak and minimum carbonate content. Another four samples were studied in order to help define the suspected Valanginian-Hauterivian stage boundary (samples BB 1–4). Standard smear slide preparation followed the conventional technique described by Bown (1998). The slides were studied at x1000 magnification under cross-polarized light using an Olympus BX51 microscope with an oil immersion objective. For each sample, 40 fields of view were scanned and the number of complete, non-fragmented coccoliths counted to quantify total nannoplankton abundance (Table 1).

3.6. Ammonoids

During the fieldwork in 2014 and 2015, no systematic fossil collection was performed, but several ammonoid specimens were collected both *ex situ* and *in situ* from Section I. The biostratigraphic subdivision of Section II is based on a small-scale but systematic ammonoid collection, which yielded about two dozen ammonoids below the “green marker bed” (Főzy, 1995). The cephalopod fauna of Sections I and II is comparable with the fauna of the lower part of Section III, more specifically with Section C of Főzy and Janssen (2009). This section comprises beds labelled from 200 to 258, and yielded 1660 fossil cephalopod specimens, collected bed-by-bed, which served as a solid foundation for biostratigraphy. Undoubtedly, this fauna originates from below the "green marker bed" (Fig. 2 in Főzy and Janssen, 2009); however, due to the lack of detailed documentation of the collection, its precise position remains uncertain.

3.7. X-ray fluorescence measurements

X-ray fluorescence (XRF) measurements were made on a suite of 8 samples to estimate the carbonate content of beds with different lithologies. A total of 20 elements were analysed with a Thermo Scientific Niton XL3t 900 GOLDD+ portable XRF analyser, equipped with a 50 kV X-ray tube and a silver target anode, at the Research Centre for Natural Sciences, Hungarian Academy of Sciences, Budapest. For quantitative analysis, the standardless fundamental parameters method was used with Compton-normalization. For data evaluation, Excel and Statistica 12 software was used. The $CaCO_3$ content was calculated from the XRF data by multiplying the Ca_{XRF} content, given in weight percent, by 2.5. The standard error of the Ca_{XRF} measurements is lower than 0.2 wt%.

4. Results

4.1. Stable isotope analyses

At the Bersek Quarry section, the bulk carbonate $\delta^{13}C_{VPDB}$ values range from 0.2‰ to 3.6‰, with an average of 2.6‰ (Fig. 2). The isotope curve can be divided into two parts on the basis of long-term trends. From 0 m to 19.2 m above the base of the section, the curve is stable with no long-term trend, with values oscillating between 1.6‰ and 3.6‰ and an average value of 2.7‰. The second part of the curve, starting from 19.4 m above the base, displays a decreasing trend, with values dropping to a range between 2.8‰ to 0.2‰.

The bulk carbonate $\delta^{18}O_{VPDB}$ values vary between -5.6‰ and -1.3‰, with an average of -2.7‰ (Fig. 2). The curve shows a slight trend towards increasing values. These negative values are depleted compared to unaltered marine calcite (van de Schootbrugge et al., 2000). The slight covariance of $\delta^{13}C$ and $\delta^{18}O$ values suggests some degree of diagenetic overprint. As the oxygen isotopes are generally more prone to alteration than the carbon isotope values (Sprovieri et al., 2006), we interpret only the latter in the following discussion.

4.2. Magnetic susceptibility measurements

The magnetic susceptibility values fall between 6.266x10^{-8} m^3/kg and 125.01x10^{-6} m^3/kg, with an average of 44.781x10^{-8} m^3/kg (Fig. 2). Three samples (BQ4, BQ17, and BQ37) show values over 160x10^{-8} m^3/kg and are considered as outliers as they contain sand grains originating from nearby turbidite beds, disturbing the information from the pelagic chronic sedimentation. Three minima can be found at 3 m, 10 m, and 14.5 m. No distinctive long-term drift can be observed in the magnetic susceptibility values.

4.3. Gamma-ray spectroscopy

The gamma-ray spectroscopy values fall between 27.5 Ue ppm and 46.8 Ue ppm (Fig. 2). As the organic matter content does not change significantly in the studied section and the turbidite beds are too rare and thin to considerably change the measured values, the gamma-ray values produced here are considered to reflect the changes in the detrital vs. carbonate contribution in the sediment. The minima of the gamma-ray spectroscopy curve are located at the same stratigraphic levels as those in the magnetic susceptibility curve. The gamma-ray spectroscopy curve shows a long-term trend toward slightly decreasing values.

4.4. Time series analyses for cyclostratigraphy

The power spectrum of the magnetic susceptibility signal shows spectral peaks over the 99% confidence level (CL) with periods of 5.12 m and 0.23 m, and over the 95% CL with periods of 1.60 m and 0.28 m (Fig. 3A). Other peaks exceed the 90% CL with periods of 0.56 and 0.40 m, but do not reach the 95% CL. As they are observed in the other proxies and in the evolutive spectral analyses, these peaks will be discussed in the following sections of the manuscript. In the spectrogram focusing on the low frequencies (Fig. 4H), the peak centred on 5.12 m is detected throughout the series with the highest spectral power around 12 m above the base of the section. This band first increases from 3.8 m to 7.9 m, from the base of the section to 6 m above the base, and then decreases to ~5 m, towards 15 m above the base. In the spectrogram focusing on the high frequencies (Fig. 4I), the peak centred on 1.60 m first shows a bifurcation to two periods at 1.6 m and 0.9 m, from the base of the section to 5 m above the base. After an interval from 5 m to 7 m above the base of the section, the band appears again from 7 m to 13 m above the base, with a period evolving from 1.3 m to 1.9 m. In the upper part of the section, the expression of this band is observed with a period of 0.9 m. The peaks of periods 0.23 m and 0.28 m appear from 4 m to 13 m above the base of the section. Another band of periods is observed with periods ranging from 0.4 m to 0.6 m at 5 m, 13 m and 16 m above the base of the series.

The power spectrum of the gamma-ray spectroscopy signal shows peaks over the 99% CL with periods of 5.12 m and 0.81 m (Fig. 3B). A peak with a period of 0.57 m reaches the 95% CL. Another peak is observed with a period of 1.60 m over the 90% CL. Although this peak does not reach the 95% CL, we will discuss the expression of this peak on the spectrograms. No significant peak with periods shorter than 0.3 m can be recognised because, irrespective of the 0.1 m sample step, the measurements cannot be regarded pointwise. Due to its size, the detector collects 95% of the signal from a 0.3 m radius which smoothens the short-term signal and increases the effective Nyquist-frequency of the GRS signal. In the spectrogram focusing on the low frequencies (Fig. 4E), the cyclicity band centred on 5.12 m is observed throughout the series with high spectral power. Its period increases from 4.8 m to 7.0 m from the base of the section to 7 m above the base, and then decreases to 3.0 m towards 16 m above the base. In the spectrogram focusing on the high frequencies (Fig. 4F), the cyclicity band centred on 1.60 m is apparent throughout the section, with periods ranging from 2.0 m to 0.9 m. The band centred on 0.57 m appears from 2.5 m to 6.5 m above the base of the section.

The power spectrum of the $\delta^{13}C$ signal shows cyclicities over the 99% CL with periods of 0.59 m, 0.32 m, and 0.21 m, and peaks over the 95% CL with periods of 5.23 m, 1.96 m, 0.74 m and 0.29 m (Fig. 3C). In the spectrogram focused on low frequencies (Fig. 4B), the cyclicity band centred on 5.23 m is observed with high amplitudes from the base of the section to 9 m above the base, and from 18 m above the base to the top of the section. From 10 m to 18 m above the base of the section, this band has much lower amplitudes. Its period varies between 5.7 m and 5.1 m. On the spectrogram focused on the high frequencies (Fig 4C), the band centred on 1.96 m is observed from the base of the section to 3 m with a period of 1.8 m. It appears transiently around 14 m and 19 m above the base of the section, with periods of 1.7 m and 2.2 m, respectively. It then appears as a continuous band from 23 m to the top of the series. The band with periods ranging from 0.74 m to 0.58 m first appears around 6 m above the base of the section with a period of 0.8 m. It is then observed from 8 m to 12 m above the base of the section with two periods of 0.8 m and 0.6 m. It reaches the highest amplitudes from 15 m to 27 m above the base of the section. In this interval, this band has periods decreasing from 0.8 m to 0.6 m. It is then expressed from 28 m above the base to the top of the section with a period of 0.9 m. The band of periods ranging from 0.32 m to 0.29 m appears between 8 m and 12 m above the base of the section. The peak centred on 0.43 m is observed with low amplitudes around 3 m and 18 m above the base of the section.

Comparing the power spectra with the spectrograms of the three signals distinguishes three periodicity bands. The most prominent periodicity in all three signals appears in the spectrograms focusing on the high frequencies with a mean period of ~5 m. The peaks at 1.60 m and 1.96 m form the next band of periods, with a mean period of ~1.7 m. The peaks ranging from 0.95 m to 0.43 m are only apparent in the GRS and the $\delta^{13}C$ signals and have a mean period of ~0.6 m. The peaks ranging from 0.32 m to 0.21 m are only apparent in the magnetic susceptibility and the $\delta^{13}C$ signals and has a mean period of ~0.3 m.

4.5. Calcareous nannoplankton

Nannoplankton in the studied samples have low abundance and medium to poor preservation. Reworking appears negligible despite the presence of fragmentary specimens. Diagenetic overprint, not uncommon for Cretaceous assemblages of a similar old age, is manifest in partial dissolution of specimens. The predominant taxa belong to the cosmopolitan genera *Watznaueria* and *Nannoconus* which are also abundant in other Tethyan localities (e.g., Duchamp-Alphonse et al., 2007).

For nannofossil-based biostratigraphic assignment and recognition of marker taxa, the zonal scheme of Bown (1998) was used. The presence of marker taxa and recognized first and last appearance datum (FAD and LAD) events allow recognition of nannoplankton zones NK3-NC4 throughout the studied section, whereas diagnostic species of the younger NC4-NC5 Zones are absent. Key marker species whose presence proves the NK3 and NC4 Zones are *Calcicalathina oblongata* (occurring in all samples) and *Cruciellipsis cuvillieri*. Subzone-level subdivision within the zones NK3 and NC4 is not possible as it would require recognition of marker taxa *Eiffellithus windii, Rucinolithus wisei* and *Eiffellithus striatus*, none of which have been identified within Section I. Another notable absence is that of *Tubodiscus verenae*, the marker species used elsewhere to determine the boundary between nannoplankton zones NK3 and NC4. Thus, the combined use of NK3-NC4 Zones are recommended, suggesting that the most likely chronostratigraphic assignment of Section I is the upper Valanginian, possibly ranging into the lower Hauterivian.

4.6. Ammonoids

As Section I, the focus of this study, and Section II (Főzy, 1995) are situated close to each other in the same quarry yard, it is not surprising that they represent very similar stratigraphic ranges for the "grey marlstone" and "purple marlstone" strata below the "green marker bed". These ranges include the Upper Valanginian, and possibly extend into the lowermost Hauterivian. Some of the most diagnostic ammonoids of these sections are illustrated in Fig. 5. However, Section III (Főzy and Janssen, 2009) is more complete below the "green marker bed" and represents, at least partially, most of the higher Hauterivian ammonoid zones, including the *Crioceratites loryi*, *Subsaynella sayni*, *Plesiospitidiscus ligatus*, *Balearites balearis,* and *Pseudothurmannia ohmi* Zones.

4.7. X-ray fluorescence measurements

Elemental geochemistry measurements were conducted primarily to determine the carbonate content of the marlstone and its relationship to the lithology and the nannoplankton abundance (Table 1). The carbonate content of the beds in the "grey marlstone" is quite consistent, fluctuating around 65%. On the contrary, in the "purple marlstone" the contrast between the strata is more pronounced, changing from around 40% in the clay-rich beds to as high as 90% in the calcareous beds. In both units, the carbonate content and the total nannoplankton abundance show a strong positive correlation (R^2=0.99).

5. Discussion

5.1. Biostratigraphy

The ammonoid fauna at the Bersek Quarry has a clear Mediterranean affinity that can be compared with the well-documented cephalopod assemblages of sections in the Vocontian Basin and the Provence Platform in France (Reboulet, 1995), the Betic Cordillera in Spain (Company et al., 2003), and the Northern Calcareous Alps in Austria (Lukeneder, 2005). In Sections I, II and III, long-ranging phylloceratids and lytoceratids are the most common forms, but these do not allow a precise biostratigraphic subdivision. However, in Sections I and II, the occurrence of *Oosterella* and large olcostephanids (e.g., *Olcostephanus densicostatus*) is diagnostic and indicates a Late Valanginian to earliest Hauterivian age. The neocomitids in these sections (e.g., *Neocomites neocominesis, Teschenites subflucticulus* and *Teschenites callidiscus*) are also assigned to the Valanginian. *T. callidiscus*, found only in an *ex situ* block, is the index form of the uppermost Valanginian *T. callidiscus* Zone of Reboulet (1995), the equivalent of the *T. callidiscus* Subzone of the *Criosarasinella furcillata* Zone in Reboulet et al. (2014). Section III, described in detail in Főzy and Janssen (2009), is more biostratigraphically complete. Most of the Hauterivian ammonoid zones were, at least partially, documented from the sequence of marlstone below the "green marker bed" (Főzy and Janssen, 2009). In the lower part of Section III, the common appearance of the large- and small-sized olcostephanids (*Olcostephanus densicostatus and Olcostephanus nicklesi*) is diagnostic. The middle and upper part of this section is characterized by the abundance of crioceratids (including *Crioceratites nolani* and *Crioceratites duvali*). The genera *Abrytusites* and *Plesiospitidiscus* appear in the upper part of the Section III. Also important is the occurrence of some rare, but stratigraphically important taxa, such as *Olcostephanus jeannoti, Subsaynella sayni*, and *Subsaynella mimica*, *Euptychoceras meyrati* and *Pseudothurmannia ohmi*.

The bloom of the representatives of the family Holcodiscidae, characterised by a smooth band on the ventrolateral region (e.g., *Jeanthieuloyites* spp.), is a unique feature of the Bersek fauna and was observed in all three sections. Such an abundance of the *Spitidiscus*-related species is unknown from the classical Upper Valanginian sections in France (Reboulet, 1995), but were reported by Avram (1995) from the Carpathians.

The comparison of the ammonoid faunas of the three Bersek Quarry sections reveals that Section I and II are Late Valanginian or Late Valanginian to earliest Hauterivian in age, whereas Section III also includes younger strata up to the Upper Hauterivian strata. This difference can be explained by the submarine erosion during deposition of the "green marker bed", that removed the unconsolidated Middle to Upper Hauterivian layers of sediment from Sections I and II.

A crucial issue is the lack of *Acanthodiscus radiatus,* the zonal index of the lowermost Hauterivian *Acanthodiscus radiatus* Zone, which appears mainly in the successions of platform deposits in southeast France (e.g., Reboulet, 1995). This species is missing from the deeper water fauna recovered at the Bersek Quarry. Nevertheless, the Valanginian/Hauterivian boundary can be drawn in Section III. The coeval first appearance of the genus *Saynella* (represented by a big, smooth specimen) and *Olcostephanus hispanicus,* together with the bloom of the genus *Crioceratites,* suggests that the boundary can be placed between Bed 236 and Bed 237 (Főzy and Janssen, 2009). These ammonoids were absent in Section I and II, where fewer total fossils were collected. Therefore, the Valanginian/Hauterivian boundary cannot be confidently drawn in these sections, but the possibility of its presence cannot be excluded.

Our nannoplankton biostratigraphic results are in good agreement with those drawn from the ammonoids and concur with the conclusions of previous studies by

Fogarasi (1995b, 2001) and Főzy and Fogarasi (2002), which were based on significantly larger sampling (130 smear slides) and documented the presence of 63 nannofossil taxa from Section III. These earlier semi-quantitative analyses also observed the dominance of common Tethyan forms such as *C. oblongata, Nannoconus* sp. and *W. barnesiae*. Although many Tethyan marker species were reported and permit biostratigraphic assignment from the NK3 Zone upwards, two key taxa for defining zone and subzone boundaries, *T. verenae* and *Lithraphidites bollii*, have not been reliably recorded (Főzy and Fogarasi, 2002). However, in Section III, Fogarasi (2001) documented the successive LADs of two marker species that range though Section I in our samples, *C. cuvillieri* and *C. oblongata*, thus establishing that deposition of the Bersek Marl Formation continued into nannoplankton zone NC5, and the "green marker bed" is best assigned to the NC5b-c Subzones. Thus, the nannoplankton biostratigraphic evidence also suggest that the base of the "green marker bed" is erosive and the topmost "purple marlstone" layers are highly diachronous between sections I and III, being not younger than earliest Hauterivian in the former, and as young as Late Hauterivian in the latter.

5.2. Recognition of the Weissert Event

The shape of the bulk carbonate $\delta^{13}C$ curves during the Weissert Event are similar across most of the previously reported sections (Price et al., 2016). At the Early–Late Valanginian transition, the $\delta^{13}C$ values rise steeply to values that are approximately 1–2‰ higher than before the onset. After this increase, a plateau phase of elevated $\delta^{13}C$ values is observed, that is followed by a slow and gradual decline. During the

Valanginian and Hauterivian, the plateau of the Weissert Event is the only interval where the $\delta^{13}C$ values stabilise at high values (Price et al., 2016).

The $\delta^{13}C$ curve of the Bersek Quarry shows elevated values around 2.7‰ until an inflexion point at 19.2 m above the base of the section. From there on, the values are gently decreasing. The good preservation of the orbital cyclicities supports the primary origin of the high values and the overall trends (see also discussion in Pellenard et al., 2014). Therefore, based on the inferred latest Valanginian/earliest Hauterivian age of the Bersek Quarry section, it is reasonable to interpret the inflexion in the bulk carbonate $\delta^{13}C$ curve as marking the termination of the plateau phase of the Weissert Event.

5.3. Astronomically forced cyclic changes in the record

The ratio of the observed three key periodicities to each other (5.1:1.7:0.6:0.2–0.3) is broadly similar to the ratio of the mean long eccentricity, short eccentricity, obliquity, and precession periods (405:100:36.6:21), according to the La2004 model (Laskar et al., 2004). Therefore, the recognised ~5 m, ~1.7 m, ~0.6 m, and ~0.2–0.3 m periods are interpreted as the 405-kyr ("long") eccentricity, the 100-kyr ("short") eccentricity, the obliquity, and the precession cycles, respectively.

To test this interpretation, the magnetic susceptibility, the gamma-ray spectroscopy signals, and the lower part of the $\delta^{13}C$ signal were calibrated using the proposed short eccentricity signal filtered from the magnetic susceptibility signal, in which 12 complete short eccentricity cycles can be counted (Fig. 4J-L). The magnetic susceptibility is used here as a reference because the high resolution of this signal allows the detection of short periods, unlike the GRS signal, so that the evolution of the short eccentricity can be monitored throughout the series on spectrograms (Fig. 4I). In addition, the eccentricity cycles appear continuous on spectrograms of the magnetic susceptibility signal, unlike the $\delta^{13}C$ signal (Fig. 4C). However, at levels 1.6 m, 5.7 m and 10.5 m the evolutive spectrum of the MS series shows bifurcation in the short eccentricity band (Fig. 4I), so that its evolution is unclear.

The power spectrum of the tuned magnetic susceptibility signal shows prominent peaks at 360 kyr, 105 kyr, and 41 kyr (Fig. 3D). These are nearly identical to the expected periods of the long eccentricity, short eccentricity, and the obliquity cycles. The other peak at 29 kyr can be a consequence of short-term variations of the sedimentation rate or a consequence of aliasing in intervals showing lower sedimentation rates. The power spectrum of the tuned gamma-ray spectroscopy signal shows prominent peaks at 360 kyr, 109 kyr, and 41 kyr, that corresponds to the long eccentricity, short eccentricity, and obliquity periods, respectively (Fig. 3E). The power spectrum of the tuned $\delta^{13}C$ signal shows prominent peaks at 500 kyr, 106 kyr, and 42 kyr, reasonably representing the long eccentricity, the short eccentricity, and the obliquity periods, respectively (Fig. 3F).

The amplitude modulation of the 100-kyr band filtered in the magnetic susceptibility signal was further investigated. To define the amplitude modulation of the proposed short eccentricity signal, Hilbert transform was applied to the tuned band-passed signal (Fig. 6; Meyers, 2014). The enveloping amplitude modulation signal shows maxima roughly coinciding with the maxima of the proposed long eccentricity signal filtered from the magnetic susceptibility (Fig. 6A). The main peak on the corresponding 2π-MTM power spectrum has mean period of 418 kyr, close to the period of the 405-kyr eccentricity cycle (Fig. 6B). The main modulator of the short eccentricity signal in geological time series is the long eccentricity. The close relationship between the amplitude modulation signal of the presumed short eccentricity signal and the presumed long eccentricity signal reinforces our cyclostratigraphical interpretation.

5.4. Sedimentation rate

The average sedimentation rate at the lower part of the Bersek Quarry section is 14 m/Myr. It varies between 9–19 m/Myr, with maxima around 1 m, 6 m, and 13 m above the base of the section. The band-pass filter output signals corresponding to the long eccentricity signal are identified in the same phase in the gamma-ray spectroscopy and the magnetic susceptibility datasets, with maxima around 1 m, 6 m, and 14 m above the base of the section (Fig. 8). These maxima almost coincide with the maxima of the sedimentation rate. The first two long eccentricity cycles in the $\delta^{13}C$ signal appear to be in antiphase compared to the magnetic susceptibility and gamma-ray spectroscopy signals, but then become in-phase with them around 15 m above the base. In this part of the section, the amplitude of the long eccentricity filter output signal is low, therefore it is likely that the shift in the phase is only apparent and does not result from palaeoenvironmental changes.

The plateau phase of the Weissert Event in the Bersek Quarry section spans until 19.2 m above the base. It was shown, that the deposition of lowermost 16.8 m of the section took approximately 1.25 Myr. It is regarded here as a minimum estimate for the plateau phase of the Weissert Event, since the entire plateau phase is likely not preserved here and not all the preserved interval is included in this interval. Our minimum duration estimate nonetheless agrees with the durations calculated in contemporaneous sections (e.g. Martinez et al., 2015).

The average 10 m/Myr sedimentation rate estimated by Fogarasi (1995b) falls within the range of our results. He suggested that the 0.2-m thick marlstone-limestone couplets could indicate precession cycles. According to our calculations, a marlstone-limestone couplet driven by precession forcing should be approximately 0.1–0.3 m thick. This is also the variation that is observable in the field in the “purple marlstone” unit. The average sedimentation rate during the Late Valanginian–Early Hauterivian in the Gerecse Mountains is significantly lower than in the Vocontian Trough. The average sedimentation rate during this time at the Orpierre and the La Charce/Vergol/Morenas sections is around 48 m/Myr (Charbonnier et al., 2013; Martinez et al., 2013), and at the Angles/Reynier section is around 40 m/Myr (Martinez et al., 2013). In the Capriolo section, located in the Umbria-Marche Basin, a sedimentation rate of 17 m/Myr was calculated for the Late Valanginian–Early Hauterivian, which is comparable to our results (Sprovieri et al., 2006).

5.5. Impact of the sample distance on the cyclostratigraphic interpretations

The precession cycles have shown to have periods close to the detection limit of our measured series (Fig. 3). Low-density sampling in the studied time series can cause distortion of the spectrum in the precession band, making the record of the orbital cycles unclear (Weedon, 2003). Furthermore, a highly fluctuating sedimentation rate can smooth the power spectrum at high frequencies and decrease the power and significance levels of the spectral peaks in an important proportion of the spectrum (see Martinez et al., 2016). The effect of the low-density sample distance, and the variations in the sedimentation rate on the spectral analyses were tested on four ETP (Eccentricity - Tilt - Precession) series calculated for the Late Valanginian using the La2004 (Laskar et al., 2004) solution (Fig. 7). Three modelled ETP series represent a hypothetical section with a sedimentation rate of 14 m/Myr, analogous to the Bersek Quarry section, sampled every 0.05 m, 0.1 m and 0.2 m. A fourth ETP series of the same hypothetical section, sampled every 0.01 m, is regarded to be the ideal representation of the astronomical cycles.

On the power spectrum corresponding to the 5-kyr and the 10-kyr sample distances, the peaks associated with the long and the short eccentricity, the obliquity, and the precession cycles are present (Fig. 7A-B). However, on the power spectrum corresponding to the 20-kyr sample distance, the peaks associated with the precession cycles are absent (Fig. 7C). Compared to the power spectrum of the ideal ETP series, the obliquity and eccentricity signals are not impacted by aliasing when analysing the ETP series sampled at a resolution of 5 kyr and 10 kyr. When analysing the ETP series sampled with a resolution of 20 kyr, significant changes in power occur at all Milankovitch-band (Fig. 7C), so that the amplitude of the eccentricity band is affected. The series sampled at 10 kyr thus still allows a correct reconstruct of the amplitude of the eccentricity cycles.

The effect of a fluctuating sedimentation rate was tested by setting a sedimentation rate cyclically fluctuating from 9 m/Myr to 19 m/Myr with maxima coinciding with the maxima of the long eccentricity to the previously described ETP series. On the power spectra of the modelled signals, the dispersion of the frequencies is apparent, but the Milankovitch-cyclicities remain detectable (Fig. 7D-F). In particular, at 0.05 m and 0.1 m, the power spectra do not significantly differ from the power spectrum of the ETP series sampled 0.01 m (Fig. 7D-E). Our test results imply that in a hypothetical section that is analogous with the Bersek Quarry section, a proxy signal sampled with a sample step of 0.1 m is capable of recording the long and the short eccentricity, the obliquity, and the precession. Even with a high variation in the sedimentation rate, our sensitivity analysis demonstrates that the long and the short eccentricity signals remain sufficiently well preserved to support our interpretation that the high-power peaks at the high-frequency end of the power spectrum of the $\delta^{13}C$ and the magnetic susceptibility signals are feasibly associated with the precession cycles in the lower part of the studied section. A proxy signal sampled with an average sample step of 0.2 m, representative of the upper 14.4 m section sampling protocol, is capable to record the long and the short eccentricity and the obliquity, with however large disturbances in the amplitude of these cycles compared to the series sampled at 0.01 m (Fig. 7F). These tests show that the interval of the series sampled at 0.1 m is suitable for the recognition of the actual amplitude of the eccentricity cycles and thus viable for astronomical tuning.

5.6. Origin of the cyclicities in the record

The origin of the observed Milankovitch cyclicities in the measured proxy signals is most likely related to the variation in terrestrially-derived detrital input (e.g., Cotillon, 1987; Mutterlose & Ruffell, 1999; Reboulet et al., 2003; Martinez et al., 2015; Lukeneder et al., 2016). The intensification of the hydrological cycle typical during more humid periods is likely to correspond to an increase in detrital material. This contributes to the elevated gamma-ray spectroscopy and magnetic susceptibility values, with coinciding maxima and minima, respectively. The increased nutrient availability, resulting from enhanced terrestrial input, supports elevated primary production and subsequently decreases the bulk carbonate $\delta^{13}C$ values. Hence, it explains the inverse correlation between the $\delta^{13}C$ and the MS-GRS signals. The maxima of the sedimentation rate at the studied section concur with the maxima of the long eccentricity in the MS-GRS signals, implying that the sedimentation rate is linked to orbital forcing (Fig. 8). Furthermore, in the "purple marlstone" the $\delta^{13}C$ values and the carbonate content show a positive correlation. Since low carbonate content is characteristic of a humid climate with high runoff rate, a decrease in $\delta^{13}C$ values agrees with the dilution model (e.g., Fogarasi, 1995).

The response of the sedimentary record to the climatic variations is similar across the Tethyan realm, and has been observed in the Vocontian Basin (SE France; Cotillon, 1987), in the Lower Saxony Basin (NW Germany; Mutterlose & Ruffell, 1999), and in the Subbetic Domain (SE Spain; Moiroud et al., 2012). In these geological settings, the more argillaceous beds were deposited under a humid climate with high continental runoff, whereas the beds with a higher carbonate content indicate a semi-arid climate with a lower continental detrital influx (Mutterlose & Ruffell, 1999; Moiroud et al., 2012). These variations have been observed at both the small scale (i.e., precession or obliquity controlled bed couplets) and larger scale (i.e., eccentricity controlled bed bundles). Migration of carbonates from the originally more clay-rich to the more calcareous beds during the early diagenesis processes has been notably invoked to explain the onset of the marl–limestone alternations (Munnecke et al., 2001). However, the bundling of the climatic cycles into small and larger scales in the above-mentioned geological settings and the fact that clay minerals (insoluble and related to changes in humidity levels) follow the bundling between the precession and the eccentricity cycles strongly supports an orbital control on the Tethyan marlstone-limestone alternations via humid-arid cycles (Cotillon, 1987; Mutterlose & Ruffell, 1999; Martinez et al., 2015).

At the Bersek Quarry, the carbonate content and the total nannoplankton abundance in both the "grey marlstone" and the "purple marlstone" show a strong positive correlation. This implies that the carbonate content is highly dependent on nannoplankton production. Even if carbonate migration might have happened, it did not have a significant effect on the lithology. Conversely, the lithological cycles follow the pattern of the orbital forcing. Even the sedimentation rate appears to follow the filter of the long eccentricity cycle, which support the link between the marl-limestone alternations of the Gerecse Mountains and humid-arid cycles orbitally forced.

6. Conclusions

In this study, a multi-proxy approach was used to assess a local sedimentary record of the globally important Weissert Event. Bulk carbonate carbon and oxygen stable isotope measurements, gamma-ray spectroscopy and magnetic susceptibility analyses were carried out in a 31.2 m thick section at the Bersek Quarry, type locality of the Bersek Marl Formation, in the Gerecse Mountains, Transdanubian Range, Hungary. A Late Valanginian to possibly earliest Hauterivian age of the section is confirmed by ammonoid and calcareous nannoplankton biostratigraphy. Cyclostratigraphic analyses performed on all the studied proxy signals suggest an average sedimentation rate of 14 m/Myr. Based on the preservation of Milankovitch-cyclicity and comparison with other Tethyan sections, the values and trend of the $\delta^{13}C$ signal are considered to reflect a primary signal. The inflexion point of the $\delta^{13}C$ curve, where the sustained plateau of high values transitions to a decreasing trend, is interpreted as the termination of the plateau phase of the Late Valanginian Weissert Event. The plateau phase of the Weissert Event as recorded in the Bersek Quarry section is at least 1.4 Myr in duration, in agreement with the range of estimates obtained throughout the Tethyan realm. The proxy signals and the sedimentary pattern of the Bersek Marl Formation suggest the presence of dilution cycles which fits the model established for Tethyan realm and argues that orbitally forced humid-arid cycles are a major determining factor in the generation of the (hemi-)pelagic marlstone-limestone alternations during the Valanginian–Hauterivian ages.

Acknowledgements

The authors would like to thank Zs. Tilk for his assistance for permission to carry out the field work and to Holcim Hungária Ltd. for granting access to the study site. We thank C. Aubourg (Université de Pau et des Pays de l'Adour) for allowing the first author to conduct the MS analyses at the LFC-R and Z. May (Research Centre for Natural Sciences, Hungarian Academy of Sciences) for his expert help with XRF analyses. O. Sztanó is acknowledged for fruitful discussions and scientific advice. Financial support of MOL Plc. is gratefully acknowledged. We thank A. Lukeneder and an anonymous reviewer for their constructive comments that improved this manuscript. This is a MTA-MTM-ELTE Paleo contribution No. 238.

References

Adatte, T., Stinnesbeck, W., Hubberten, H., Remane, J., López-Oliva, J.G., 2001. Correlation of a Valanginian stable isotopic excursion in Northeastern Mexico with the European Tethys. AAPG Memoir 75, 371-388.

Aguirre-Urreta, B., Lescano, M., Schmitz, M.D., Tunik, M., Concheyro, A., Rawson, P.F., Ramos, V.A., 2015. Filling the gap: new precise Early Cretaceous radioisotopic ages from the

Andes. Geological Magazine 152, 557-564.

Aguirre-Urreta, M.B., Price, G.D., Ruffell, A.H., Lazo, D.G., Kalin, R.M., Ogle, N., Rawson, P.F., 2008. Southern hemisphere Early Cretaceous (Valanginian-Early Barremian) carbon and oxygen isotope curves from the Neuquén Basin, Argentina. Cretaceous Research 29, 87-99.

Amodio, S., Ferreri, V., D'Argenio, B., Weissert, H., Sprovieri, M., 2008. Carbon-isotope stratigraphy and cyclostratigraphy of shallow-marine carbonates: the case of San Lorenzello, Lower Cretaceous of southern Italy. Cretaceous Research 29, 803-813.

Árgyelán, G., 1995. A gerecsei kréta törmelékes képződmények petrográfiai és petrológiai vizsgálata (Petrographical and petrological investigations of the Cretaceons clastic sediments of the Gerecse Mountains, Hungary). Általános Földtani Szemle 27, 59-83.

Avram, E., 1995. Representatives of the Family Holcodiscidae Spath, 1924 (Ammonitina) in Rumania. Memorie Carta Geologica d'Italia 51, 11-45.

Barbarin, N., Bonin, A., Mattioli, E., Puceat, E., Cappetta, H., Greselle, B., Pittet, B., Vennin, E., Joachimski, M., 2012. Evidence for a complex Valanginian nannoconid decline in the Vocontian basin (South East France). Marine Micropaleontology 84-85, 37-53.

Barbu, V., Melinte-Dobrinescu, M.C., 2008. Latest Jurassic to earliest Cretaceous paleoenvironmental changes in the Southern Carpathians, Romania: regional record of the late Valanginian nutrification event. Cretaceous Research 29, 790-802.

Bersezio, R., Erba, E., Gorza, M., Riva, A., 2002. Berriasian-Aptian black shales of the Maiolica formation (Lombardian Basin, Southern Alps, Northern Italy): local to global events. Palaeogeography Palaeoclimatology Palaeoecology 180, 253-275.

Bown, P.R., 1998. Calcareous nannofossil biostratigraphy. British Micropalaeontological Society Publication Series, Chapman and Hall, Kluwer Academic Publishers, London, p. 315.

Channell, J.E.T., Erba, E., Lini, A., 1993. Magnetostratigraphic calibration of the late Valanginian carbon-isotope event in pelagic limestones from northern Italy and Switzerland. Earth and Planetary Science Letters 118, 145-166.

Charbonnier, G., Boulila, S., Gardin, S., Duchamp-Alphonse, S., Adatte, T., Spangenberg, J.E., Föllmi, K.B., Colin, C., Galbrun, B., 2013. Astronomical calibration of the Valanginian "Weissert" episode: The Orpierre marl–limestone succession (Vocontian Basin, southeastern France). Cretaceous Research 45, 25-42.

Charbonnier, G., Duchamp-Alphonse, S., Adatte, T., Föllmi, K.B., Spangenberg, J.E., Gardin, S., Galbrun, B., Colin, C., 2016. Eccentricity paced monsoon-like system along the northwestern Tethyan margin during the Valanginian (Early Cretaceous): New insights from detrital and nutrient fluxes into the Vocontian Basin (SE France). Palaeogeography, Palaeoclimatology, Palaeoecology 443, 145-155.

Company, M., Sandoval, J., Tavera, J.M., 2003. Ammonite biostratigraphy of the uppermost Hauterivian in the Betic Cordillera (SE Spain). Geobios 36, 685-694.

Cotillon, P., 1987. Bed-scale cyclicity of pelagic Cretaceous successions as a result of world-wide control. Marine Geology 78, 109-123.

Cotillon, P., Rio, M., 1984. Cyclic sedimentation in the Cretaceous of Deep-Sea-Drilling- Project Site-535 and Site-540 (Gulf of Mexico), Site-534 (Central Atlantic), and in the Vocontian Basin (France). Initial Reports of the Deep Sea Drilling Project 77, 339-376.

Császár, G., Árgyelán, G.B., 1994. Stratigraphic and micromineralogic investigations on Cretaceous Formations of the Gerecse Mountains, Hungary and their palaeogeographic implications. Cretaceous Research 15, 417-434.

Császár, G., Haas, J., 1984. The Cretaceous in Hungary: a review. Acta Geologica Hungarica 27, 417-428.

Csontos, L., Vörös, A., 2004. Mesozoic plate tectonic reconstruction of the Carpathian region. Palaeogeography Palaeoclimatology Palaeoecology 210, 1-56.

Duchamp-Alphonse, S., Fiet, N., Adatte, T., Pagel, M., 2011. Climate and sea-level variations along the northwestern Tethyan margin during the Valanginian C-isotope excursion: Mineralogical evidence from the Vocontian Basin (SE France). Palaeogeography Palaeoclimatology Palaeoecology 302, 243-254.

Duchamp-Alphonse, S., Gardin, S., Bartolini, A., 2014. Calcareous nannofossil response to the Weissert episode (Early Cretaceous): Implications for palaeoecological and palaeoceanographic reconstructions. Marine Micropaleontology 113, 65-78.

Duchamp-Alphonse, S., Gardin, S., Fiet, N., Bartolini, A., Blamart, D., Pagel, M., 2007. Fertilization of the northwestern Tethys (Vocontian basin, SE France) during the Valanginian carbon isotope perturbation: Evidence from calcareous nannofossils and trace element data. Palaeogeography Palaeoclimatology Palaeoecology 243, 132-151.

Erba, E., 2004. Calcareous nannofossils and Mesozoic oceanic anoxic events. Marine Micropaleontology 52, 85-106.

Erba, E., Bartolini, A., Larson, R.L., 2004. Valanginian Weissert oceanic anoxic event. Geology 32, 149-152.

Fodor, L., Sztanó, O., Kövér, S., 2013. Mesozoic deformation of the northern Transdanubian Range (Gerecse and Vértes Hills). Acta Mineralogica-Petrographica, Field Guide Series 31, 1-52.

Fogarasi, A., 1995a. Üledékképződés egy szerkezeti mozgásokkal meghatározott kréta korú tengeralatti lejtőn a Gerecse hegységben – munkahipotézis (Sedimentation on tectonically controlled submarine slopes of Cretaceous age, Gerecse Mts., Hungary - working hypothesis). Általános Földtani Szemle 27, 15-41.

Fogarasi, A., 1995b. Ciklussztratigráfiai vizsgálatok a gerecsei krétában: előzetes eredmények (Cretaceous cyclostratigraphy of Gerecse Mts: Preliminary results). Általános Földtani Szemle 27, 43-58.

Fogarasi, A., 2001. Dunántúli-középhegységi alsó-kréta képződmények mészvázú nannoplankton sztratigráfiája (Nannoplankton biostratigraphy of the Lower Cretaceous deposits in the Transdanubian Range, Hungary) (PhD thesis). Eötvös Loránd University, Budapest, Hungary.

Föllmi, K.B., 2012. Early Cretaceous life, climate and anoxia. Cretaceous Research 35, 230-257.

Föllmi, K.B., Godet, A., Bodin, S., Linder, P., 2006. Interactions between environmental change and shallow water carbonate buildup along the northern Tethyan margin and their impact on the Early Cretaceous carbon isotope record. Paleoceanography 21, PA4211.

Főzy, I., 1995. A gerecsei Bersek-hegy alsó kréta ammonitesz rétegtana (Lower Cretaceous ammonite biostratigraphy of the Bersek Hill (Gerecse Mts., Hungary)). Általános Földtani Szemle 27, 7-14.

Főzy, I., 2013. Late Jurassic–Early Cretaceous fauna, biostratigraphy, facies and deformation history of the carbonate formations in the Gerecse and Pilis Mountains (Transdanubian Range, Hungary). GeoLitera, Szeged, p. 422.

Főzy, I., Fogarasi, A., 2002. A gerecsei Bersek-hegy törmelékes sorozatának tagolása az alsó-kréta ammonitesz fauna és a nannoplankton flóra alapján (The Lower Cretaceous biostratigraphy of the Bersek Hill (Gerecse Mts., Transdanubian Range) on the basis of the ammonites and nannofossils). Földtani Közlöny 132, 293-324.

Főzy, I., Janssen, N.M.M., 2009. Integrated Lower Cretaceous biostratigraphy of the Bersek Quarry, Gerecse Mountains, Transdanubian Range, Hungary. Cretaceous Research 30, 78-92.

Főzy, I., Janssen, N.M.M., Price, G.D., Knauer, J., Pálfy, J., 2010. Integrated isotope and biostratigraphy of a Lower Cretaceous section from the Bakony Mountains (Transdanubian Range, Hungary): A new Tethyan record of the Weissert event. Cretaceous Research 31, 525-545.

Fülöp, J., 1958. A Gerecsehegység krétaidőszaki képződményei (Die kretazeischen Bildungen des Gerecse-Gebirges). Geologica Hungarica 11, 1-124.

Grădinaru, M., Lazar, I., Bucur, I.I., Grădinaru, E., Săsăran, E., Ducea, M.N., Andrăşanu, A., 2016. The Valanginian history of the eastern part of the Getic Carbonate Platform (Southern Carpathians, Romania): Evidence for emergence and drowning of the platform. Cretaceous Research 66, 11-42.

Gréselle, B., Pittet, B., Mattioli, E., Joachimski, M., Barbarin, N., Riquier, L., Reboulet, S., Pucéat, E., 2011. The Valanginian isotope event: A complex suite of palaeoenvironmental perturbations. Palaeogeography Palaeoclimatology Palaeoecology 306, 41-57.

Gröcke, D.R., Price, G.D., Robinson, S.A., Baraboshkin, E.Y., Mutterlose, J., Ruffell, A.H., 2005. The Upper Valanginian (Early Cretaceous) positive carbon-isotope event recorded in terrestrial plants. Earth and Planetary Science Letters 240, 495-509.

Haas, J., 2012. Geology of Hungary, Regional Geology Reviews. Springer-Verlag, Berlin, Heidelberg, p. 246.

Hantken, M., 1868. Lábatlan vidékének földtani viszonyai [Geology of the Lábatlan area]. A Magyarhoni Földtani Társulat Munkálatai 4, 48-56.

Hennig, S., Weissert, H., Bulot, L., 1999. C-isotope stratigraphy, a calibration tool between ammonite and magnetostratigraphy: The Valanginian-Hauterivian transition. Geologica Carpathica 50, 91-95.

Hinnov, L.A., Ogg, J.G., 2007. Cyclostratigraphy and the Astronomical Time Scale. Stratigraphy 4, 239-251.

Janasi, V.d.A., de Freitas, V.A., Heaman, L.H., 2011. The onset of flood basalt volcanism, Northern Paraná Basin, Brazil: A precise U–Pb baddeleyite/zircon age for a Chapecó-type dacite. Earth and Planetary Science Letters 302, 147-153.

Jenkyns, H.C., 2010. Geochemistry of oceanic anoxic events. Geochemistry, Geophysics, Geosystems 11.

Katz, M.E., Wright, J.D., Miller, K.G., Cramer, B.S., Fennel, K., Falkowski, P.G., 2005. Biological overprint of the geological carbon cycle. Marine Geology 217, 323-338.

Kázmér, M., 1987. A Lower Cretaceous submarine fan sequence in the Gerecse Mts., Hungary—. Annales Universitatis Scientiarium Budapestinensis de Rolando Eötvös Nominate, Sectio Geologica 27, 101-116.

Krische, O., Bujtor, L., Gawlick, H.J., 2013. Calpionellid and ammonite biostratigraphy of uppermost Jurassic to Lower Cretaceous sedimentary rocks from the Leube Quarry (Northern Calcareous Alps, Salzburg, Austria). Austrian Journal of Earth Sciences 106, 26-45.

Kujau, A., Heimhofer, U., Hochuli, P.A., Pauly, S., Morales, C., Adatte, T., Föllmi, K.B., Ploch, I., Mutterlose, J., 2013. Reconstructing Valanginian (Early Cretaceous) mid-latitude vegetation and climate dynamics based on spore-pollen assemblages. Review of Palaeobotany and Palynology 197, 50-69.

Kujau, A., Heimhofer, U., Ostertag-Henning, C., Greselle, B., Mutterlose, J., 2012. No evidence for anoxia during the Valanginian carbon isotope event-An organic-geochemical study from the Vocontian Basin, SE France. Global and Planetary Change 92-93, 92-104.

Laskar, J., Robutel, P., Joutel, F., Gastineau, M., Correia, A.C.M., Levrard, B., 2004. A long-term numerical solution for the insolation quantities of the Earth. Astronomy & Astrophysics

428, 261-285.

Lini, A., Weissert, H., Erba, E., 1992. The Valanginian carbon isotope event - a first episode of greenhouse climate conditions during the Cretaceous. Terra Nova 4, 374-384.

Littler, K., Robinson, S.A., Bown, P.R., Nederbragt, A.J., Pancost, R.D., 2011. High sea-surface temperatures during the Early Cretaceous Epoch. Nature Geoscience 4, 169-172.

Lukeneder, A., 2005. Taphonomy and stratigraphy of Early Cretaceous ammonoid mass occurrences (Late Valanginian; Northern Calcareous Alps; Upper Austria). Austrian Journal of Earth Sciences 98, 34-51.

Lukeneder, A., Sotak, J., Jovane, L., Giorgioni, M., Savian, J.F., Halasova, E., Rehakova, D., Jozsa, S., Kroh, A., Florindo, F., Sprovieri, M., 2016. Multistratigraphic records of the Lower Cretaceous (Valanginian-Cenomanian) Puez key area in N. Italy. Palaeogeography Palaeoclimatology Palaeoecology 447, 65-87.

Mann, M.E., Lees, J.M., 1996. Robust estimation of background noise and signal detection in climatic time series. Climatic Change 33, 409-445.

Martinez, M., Deconinck, J.-F., Pellenard, P., Reboulet, S., Riquier, L., 2013. Astrochronology of the Valanginian Stage from reference sections (Vocontian Basin, France) and palaeoenvironmental implications for the Weissert Event. Palaeogeography Palaeoclimatology Palaeoecology 376, 91-102.

Martinez, M., Deconinck, J.-F., Pellenard, P., Riquier, L., Company, M., Reboulet, S., Moiroud, M., 2015. Astrochronology of the Valanginian–Hauterivian stages (Early Cretaceous): Chronological relationships between the Paraná–Etendeka large igneous province and the Weissert and the Faraoni events. Global and Planetary Change 131, 158-173.

Martinez, M., Kotov, S., De Vleeschouwer, D., Pas, D., Pälike, H., 2016. Testing the impact of stratigraphic uncertainty on spectral analyses of sedimentary series. Climate of the Past

Discussions, 1-22.

Mattioli, E., Pittet, B., Riquier, L., Grossi, V., 2014. The mid-Valanginian Weissert Event as recorded by calcareous nannoplankton in the Vocontian Basin. Palaeogeography Palaeoclimatology Palaeoecology 414, 472-485.

Melinte, M., Mutterlose, J., 2001. A Valanginian (Early Cretaceous) 'boreal nannoplankton excursion' in sections from Romania. Marine Micropaleontology 43, 1-25.

Meyers, S.R., 2014. Astrochron: An R Package for Astrochronology, 0.6 ed.

Moiroud, M., Martinez, M., Deconinck, J.-F., Monna, F., Pellenard, P., Riquier, L., Company, M., 2012. High-resolution clay mineralogy as a proxy for orbital tuning: Example of the Hauterivian–Barremian transition in the Betic Cordillera (SE Spain). Sedimentary Geology 282, 336-346.

Möller, C., Mutterlose, J., Alsen, P., 2015. Integrated stratigraphy of Lower Cretaceous sediments (Ryazanian–Hauterivian) from North-East Greenland. Palaeogeography Palaeoclimatology Palaeoecology 437, 85-97.

Morales, C., 2013. Palaeoenvironmental changes through the Berriasian-Valanginian Boundary, Faculté des géosciences et de l'environnement - Institut des Sciences de la Terre. Universié de Lausanne, Lausanne, p. 190.

Morales, C., Kujau, A., Heimhofer, U., Mutterlose, J., Spangenberg, J.E., Adatte, T., Ploch, I., Föllmi, K.B., 2015. Palaeoclimate and palaeoenvironmental changes through the onset of the Valanginian carbon–isotope excursion: Evidence from the Polish Basin. Palaeogeography Palaeoclimatology Palaeoecology 426, 183-198.

Munnecke, A., Westphal, H., Elrick, M., Reijmer, J., 2001. The mineralogical composition of precursor sediments of calcareous rhythmites: a new approach. International Journal of Earth Sciences 90, 795-812.

Mutterlose, J., Ruffell, A., 1999. Milankovitch-scale palaeoclimate changes in pale-dark bedding rhythms from the Early Cretaceous (Hauterivian and Barremian) of eastern England and northern Germany. Palaeogeography Palaeoclimatology Palaeoecology 154, 133-160.

Nunn, E.V., Price, G.D., Gröcke, D.R., Baraboshkin, E.Y., Leng, M.J., Hart, M.B., 2010. The Valanginian positive carbon isotope event in Arctic Russia: Evidence from terrestrial and marine isotope records and implications for global carbon cycling. Cretaceous Research 31, 577-592.

Ogg, J.G., Ogg, G.M., Gradstein, F.M., 2016. A Concise Geologic Time Scale. Elsevier, p. 240.

Pellenard, P., Tramoy, R., Pucéat, E., Huret, E., Martinez, M., Bruneau, L., Thierry, J., 2014. Carbon cycle and sea-water palaeotemperature evolution at the Middle–Late Jurassic transition, eastern Paris Basin (France). Marine and Petroleum Geology 53, 30-43.

Price, G.D., Főzy, I., Janssen, N.M.M., Pálfy, J., 2011. Late Valanginian–Barremian (Early Cretaceous) palaeotemperatures inferred from belemnite stable isotope and Mg/Ca ratios from Bersek Quarry (Gerecse Mountains, Transdanubian Range, Hungary). Palaeogeography Palaeoclimatology Palaeoecology 305, 1-9.

Price, G.D., Főzy, I., Pálfy, J., 2016. Carbon cycle history through the Jurassic–Cretaceous boundary: A new global $\delta^{13}C$ stack. Palaeogeography Palaeoclimatology Palaeoecology 451, 46-61.

Price, G.D., Mutterlose, J., 2004. Isotopic signals from late Jurassic-early Cretaceous (Volgian-Valanginian) sub-Arctic belemnites, Yatria River, Western Siberia. Journal of the Geological Society 161, 959-968.

Reboulet, S., 1995. L'évolution des ammonites du Valanginien-Hauterivien inférieur du bassin vocontien et de la plate-forme provençale (Sud-Est de la France): relations avec la stratigraphie séquentielle. Documents des Laboratoires de Géologie Lyon 137, 1-371.

Reboulet, S., Atrops, F., 1997. Quantitative variations in the Valanginian ammonite fauna of the Vocontian Basin (southeastern France) within limestone-marl cycles and within parasequence sets. Palaeogeography Palaeoclimatology Palaeoecology 135, 145-155.

Reboulet, S., Mattioli, E., Pittet, B., Baudin, F., Olivero, D., Proux, O., 2003. Ammonoid and nannoplankton abundance in Valanginian (early Cretaceous) limestone-marl successions from the southeast France Basin: carbonate dilution or productivity? Palaeogeography Palaeoclimatology Palaeoecology 201, 113-139.

Reboulet, S., Szives, O., Aguirre-Urreta, B., Barragán, R., Company, M., Idakieva, V., Ivanov, M., Kakabadze, M.V., Moreno-Bedmar, J.A., Sandoval, J., Baraboshkin, E.J., Çağlar, M.K., Főzy, I., González-Arreola, C., Kenjo, S., Lukeneder, A., Raisossadat, S.N., Rawson, P.F., Tavera, J.M., 2014. Report on the 5th International Meeting of the IUGS Lower Cretaceous Ammonite Working Group, the Kilian Group (Ankara, Turkey, 31st August 2013). Cretaceous Research 50, 126-137.

Schlanger, S.O., Jenkyns, H.C., 1976. Cretaceous Oceanic Anoxic Events: Causes and consequences. Geologie en Mijnbouw 55, 179-184.

Sprovieri, M., Coccioni, R., Lirer, F., Pelosi, N., Lozar, F., 2006. Orbital tuning of a lower Cretaceous composite record (Maiolica Formation, central Italy). Paleoceanography 21, 1-19.

Sztanó, O., 1990. Durvatörmelékes üledékek gravitációs tömegmozgásai egy gerecsei alsókréta tengeralatti csatornakitöltő konglomerátum példáján (Gravitv movements of coarse clastics: the example of a Lower Cretaceous submarine channel-filling conglomerate in the Gerecse Mts., Hungary). Általános Földtani Szemle 25, 337-360.

Taner, M.T., 2003. Attributes Revisited. Rock Solid Images (RSI), Houston, Texas. www.rocksolidimages.com/attributes-revisited/#_Toc328470897

Thiede, D.S., Vasconcelos, P.M., 2010. Parana flood basalts: Rapid extrusion hypothesis confirmed by new $^{40}Ar/^{39}Ar$ results. Geology 38, 747-750.

Thomson, D.J., 1982. Spectrum estimation and harmonic analysis. Proceedings of the IEEE 70, 1055-1096.

Thomson, D.J., 1990. Quadratic-inverse spectrum estimates: applications to palaeoclimatology. Philosophical Transactions of the Royal Society A 332, 539-597.

Tremolada, F., Bornemann, A., Bralower, T.J., Koeberl, C., van de Schootbrugge, B., 2006. Paleoceanographic changes across the Jurassic/Cretaceous boundary: The calcareous phytoplankton response. Earth and Planetary Science Letters 241, 361-371.

Tukey, J.W., 1977. Exploratory Data Analysis. Addison-Wesley Publishing Company, p. 688.

van de Schootbrugge, B., Föllmi, K.B., Bulot, L.G., Burns, S.J., 2000. Paleoceanographic changes during the early Cretaceous (Valanginian-Hauterivian): evidence from oxygen and carbon stable isotopes. Earth and Planetary Science Letters 181, 15-31.

Vigh, G., 1984. Die biostratigrafische Auswertung einiger Ammoniten-Faunen aus dem Tithon des Bakonygebirges sowie aus dem Tithon–Berrias des Gerecsegebirges. Annales Instituti Geologici Hungarici 67, 1-210.

von Eynatten, H., Gaupp, R., 1999. Provenance of Cretaceous synorogenic sandstones in the Eastern Alps: constraints from framework petrography, heavy mineral analysis and mineral chemistry. Sedimentary Geology 124, 81-111.

Weedon, G., 2003. Time-Series Analysis and Cyclostratigraphy - Examining stratigraphic records of environmental cycles. Cambridge University Press, p. 259.

Weissert, H., Erba, E., 2004. Volcanism, CO_2 and palaeoclimate: a Late Jurassic-Early Cretaceous carbon and oxygen isotope record. Journal of the Geological Society 161, 695-702.

Weissert, H., Lini, A., Föllmi, K.B., Kuhn, O., 1998. Correlation of Early Cretaceous carbon isotope stratigraphy and platform drowning events: a possible link? Palaeogeography Palaeoclimatology Palaeoecology 137, 189-203.

Westermann, S., Föllmi, K.B., Adatte, T., Matera, V., Schnyder, J., Fleitmann, D., Fiet, N., Ploch, I., Duchamp-Alphonse, S., 2010. The Valanginian $\delta^{13}C$ excursion may not be an expression of a global oceanic anoxic event. Earth and Planetary Science Letters 290, 118-131.

Figure captions

Fig. 1.

(A) Location of the Bersek Quarry section on a generalized map of structural units in Hungary (after Haas, 2012). (B) Satellite aerial view of the Bersek Quarry (Google Earth image captured in 2014). The section studied in this paper is marked with "I". Section "II" was studied by Főzy (1995) and Fogarasi (1995b). Section "III" was studied by Főzy and Fogarasi (2002), Főzy and Janssen (2009), and Price et al. (2011). (C) Paleogeographic reconstruction of the Western Tethys area during the Jurassic/Cretaceous transition (after Csontos and Vörös, 2004). SA – Southern Alps, LAA – Lower Austroalpine Nappes, MAA – Middle Austroalpine Nappes, TI – Tirolic Nappes (part of the Northern Calcareous Alps). (D) Photograph of the studied section. The boundary between the Lábatlan Sandstone Formation and the Bersek Marl Formation is marked by the erosive "green marker bed". The Bersek Marl Formation is divided into two informal units based on the colour of the marlstone: the "grey marlstone" and the overlying "purple marlstone".

Fig. 2.

Bulk carbonate $\delta^{13}C$, $\delta^{18}O$, gamma-ray spectroscopy (GRS), and magnetic susceptibility (MS) signals measured at the Bersek Quarry. The thick lines below each signal denote the long-term trend. The inset shows the correlation between the $\delta^{13}C$ and $\delta^{18}O$ values, divided into two sets based on the trend in the $\delta^{13}C$ signal: plateau phase (0–18.2 m, circles) and slow decrease (18.3–31.2 m, squares). The asterisk marks the end of the plateau phase of the Weissert Event.

Fig. 3.

2π-MTM power spectra of the magnetic susceptibility (A), gamma-ray spectroscopy (B), and the bulk carbonate $\delta^{13}C$ (C) signals. The peaks are interpreted as the 405 kyr "long" eccentricity, the 100-kyr "short" eccentricity, the obliquity, and the precession cycles. The indicated values denote the periods of the main significant peaks in metres. The width of the filters used to separate the long eccentricity are as follows: 0–0.3516 for the magnetic susceptibility, 0–0.3906 for the gamma-ray spectroscopy, and 0–0.2930 cycles/m for the $\delta^{13}C$ signal. The width of the filters used to separate the short eccentricity are as follows: 0.5078–1.3672 cycles/m for the magnetic susceptibility and for the gamma-ray spectroscopy signals, and 0.3529–1.5294 cycles/m for the $\delta^{13}C$ signal. 2π-MTM power spectra of the tuned magnetic susceptibility (D), gamma-ray spectroscopy (E) and the bulk carbonate $\delta^{13}C$ (F) signals.

Fig. 4.

Detrended signals of the $\delta^{13}C$ (A), gamma ray spectroscopy (D), and magnetic susceptibility (G) measurements, and the corresponding filtered long eccentricity filter output signals. The first spectrograms of each signal (B, E, H) focuses on the low frequencies, while the second spectrograms (C, F, I) represent the whole spectrum. The second spectrogram is filtered, thus the frequencies of the respective first spectrograms are not represented. The inset shows the short eccentricity signals filtered form the magnetic susceptibility (J), gamma-ray spectroscopy (K), and the $\delta^{13}C$ signals (L). The 12 dotted lines indicate the age model used for the tuning. The width of the Taner-filters are shown on Fig. 3.

Fig. 5.

Representative ammonoids collected from Section I (this study) and Section II (Főzy, 2005). Figured specimens are deposited in the Department of Palaeontology and Geology of the Hungarian Natural History Museum, Budapest, with inventory numbers prefixed by “INV”. (A) *Neocomites neocomiensis*; INV. 2016.192; Section I, 14.9 m. (B) *Lytoceras* sp.; INV. 2016.193; Section I, *ex situ*. (C) *Olcostephanus* sp.; INV. 2016.194; Section I, 1.7 m. (D, E) *Jeanthieuloyites* sp.; INV. 2016.195); Section I, *ex situ*. (F) *Phyllopachyceras winkleri*; INV. 2016.196; Section I, 5.0 m. (G) *Oosterella* sp.; INV. 2016.197; Section I, *ex situ*. (H, I) *Neocomites* sp.; INV. 2016.198); Section II, Bed 26. (J) *Neolissoceras grasianum*; INV. 2016.199; Section II, Bed 26. (K) *Olcostephanus densicostatus*; (INV. 2016.200), Section II, Bed 27. (L) *Teschenites callidiscus*; INV. 2016.201; Section II, *ex situ*. (M) *Teschenites subflucticulus*; INV. 2016.202; Section II, Bed 26. (N) *Jeanthieuloyites* cf. *quinquestriatus*; INV. 2016.203; Section II, Bed 16. (O) *Jeanthieuloyites* cf. *quinquestriatus*; INV. 2016.204; Section II, Bed 28.

Fig. 6.

(A) Amplitude modulation of the short eccentricity band filtered in the tuned magnetic susceptibility signal. (B) 2π-MTM power spectrum of the amplitude modulation signal. The main peak has mean period of 418 kyr, close to the period of the 405-kyr eccentricity cycle

Fig. 7.

Sensitivity analysis of the impact of the sample step and the fluctuating sedimentation rate on cyclostratigraphic analyses: (A–C) 2π-MTM power spectra of modelled ETP series representing a Valanginian section with an average sedimentation rate of 14 m/Myr, analogous to the Bersek Quarry section. The three power spectra show the aliasing effect of an increasing (0.05–0.2 m) sample step. The shaded peaks represent the ideal spectrum showing no effect of aliasing. (D–F) 2π-MTM power spectra of the same modelled series with fluctuating sedimentation rates. The sedimentation rate was set to vary between 9–19 m/Myr with maxima coinciding with the long eccentricity maxima.

Fig. 8.

Conceptual model of cyclic oscillations measured in carbon isotope ratio and magnetic susceptibility and inferred changes in climate and sedimentation. The inverse correlation of the filtered long eccentricity in the $\delta^{13}C$ and the GRS-MS signals imply an orbitally-forced dilution model for the Bersek Marl Formation. (A) During humid periods, the increase in detrital influx contributes to the elevated sedimentation rate and MS-GRS values, and through the enhanced production rate to the low $\delta^{13}C$ values. (B) A decrease in detrital influx and hence the MS-GRS values during more arid periods induces an increase in the bulk carbonate $\delta^{13}C$ values and a decrease in the sedimentation rate.

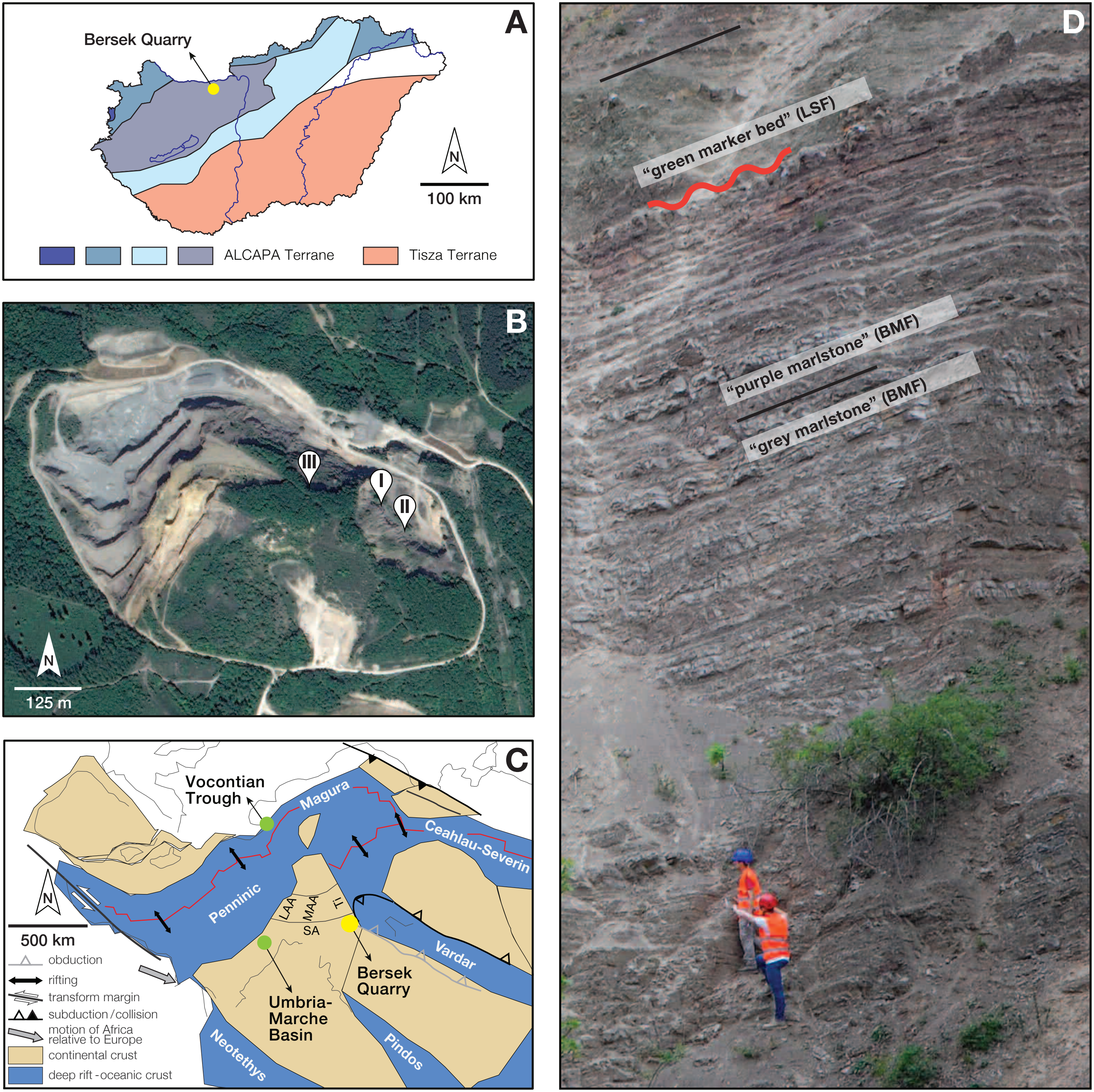
A
Bersek Quarry
N
100 km
ALCAPA Terrane
Tisza Terrane
B
III
I
II
N
125 m
C
Vocontian Trough
Magura
Ceahlau-Severin
Penninic
LAA
MAA
TI
SA
Vardar
N
500 km
obduction
rifting
transform margin
subduction / collision
motion of Africa relative to Europe
continental crust
deep rift - oceanic crust
Umbria-Marche Basin
Bersek Quarry
Neotethys
Pindos
D
"green marker bed" (LSF)
"purple marlstone" (BMF)
"grey marlstone" (BMF)

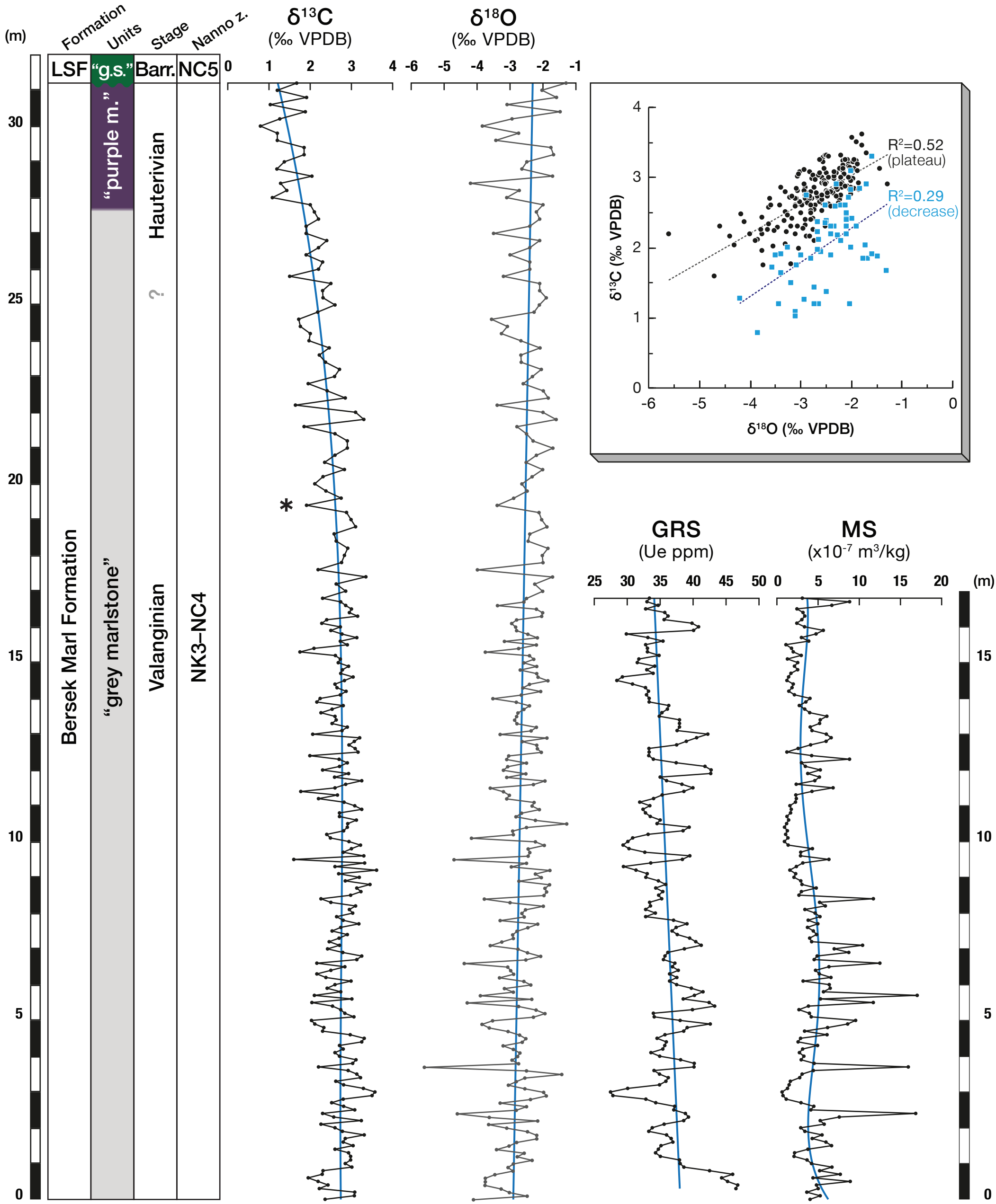
(m)
Formation
Units
Stage
Nanno z.
LSF
"g.s."
Barr.
NC5
"purple m."
Hauterivian
?
Bersek Marl Formation
"grey marlstone"
Valanginian
NK3–NC4
δ13C (‰ VPDB)
δ18O (‰ VPDB)
R²=0.52 (plateau)
R²=0.29 (decrease)
δ13C (‰ VPDB)
δ18O (‰ VPDB)
GRS (Ue ppm)
MS (x10⁻⁷ m³/kg)
*

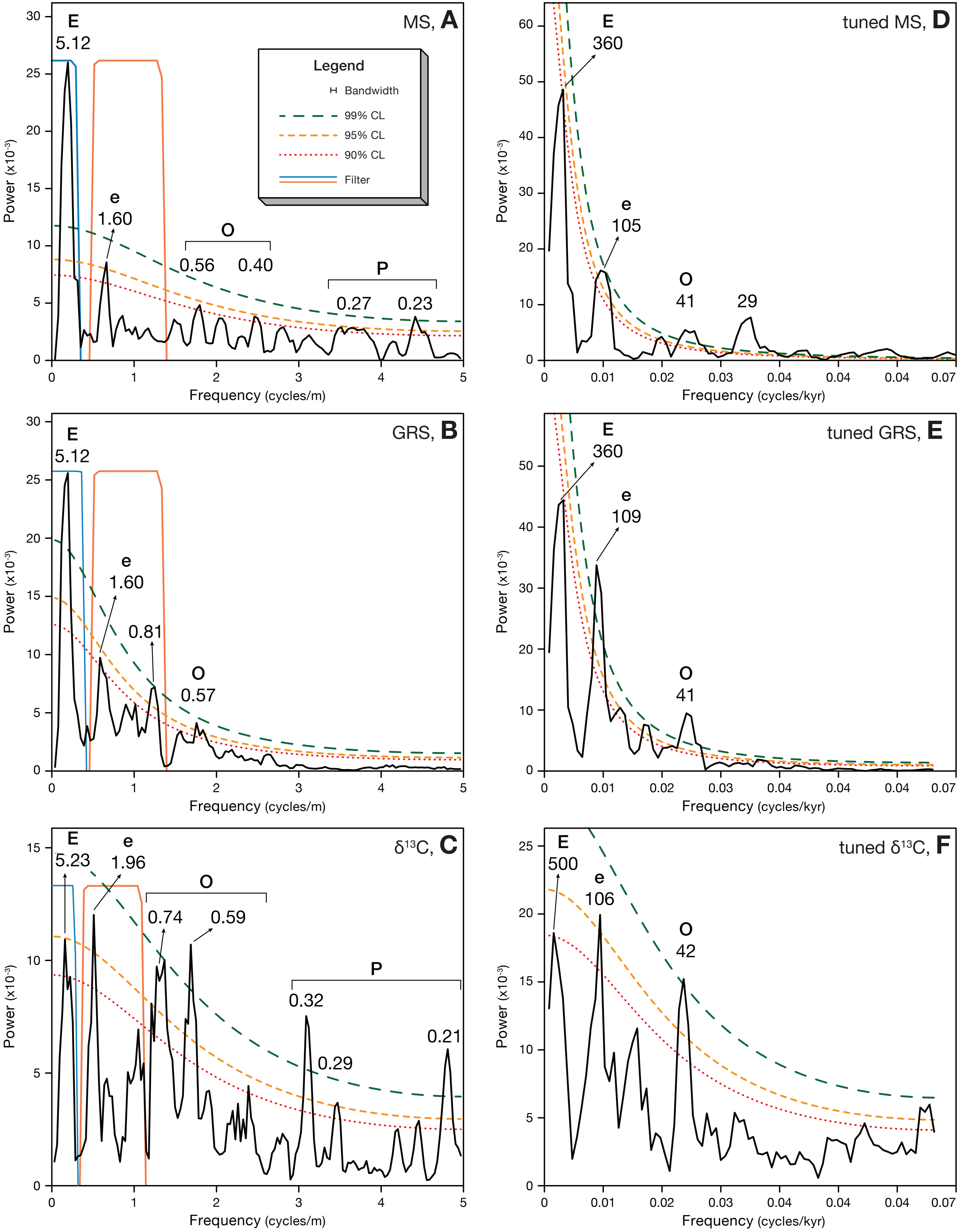

MS, A
GRS, B
δ13C, C
tuned MS, D
tuned GRS, E
tuned δ13C, F
Legend
Bandwidth
99% CL
95% CL
90% CL
Filter
E
5.12
e
1.60
O
0.56
0.40
P
0.27
0.23
0.81
0.57
5.23
1.96
0.74
0.59
0.32
0.29
0.21
360
105
41
29
109
500
106
42
Power (x10-3)
Frequency (cycles/m)
Frequency (cycles/kyr)

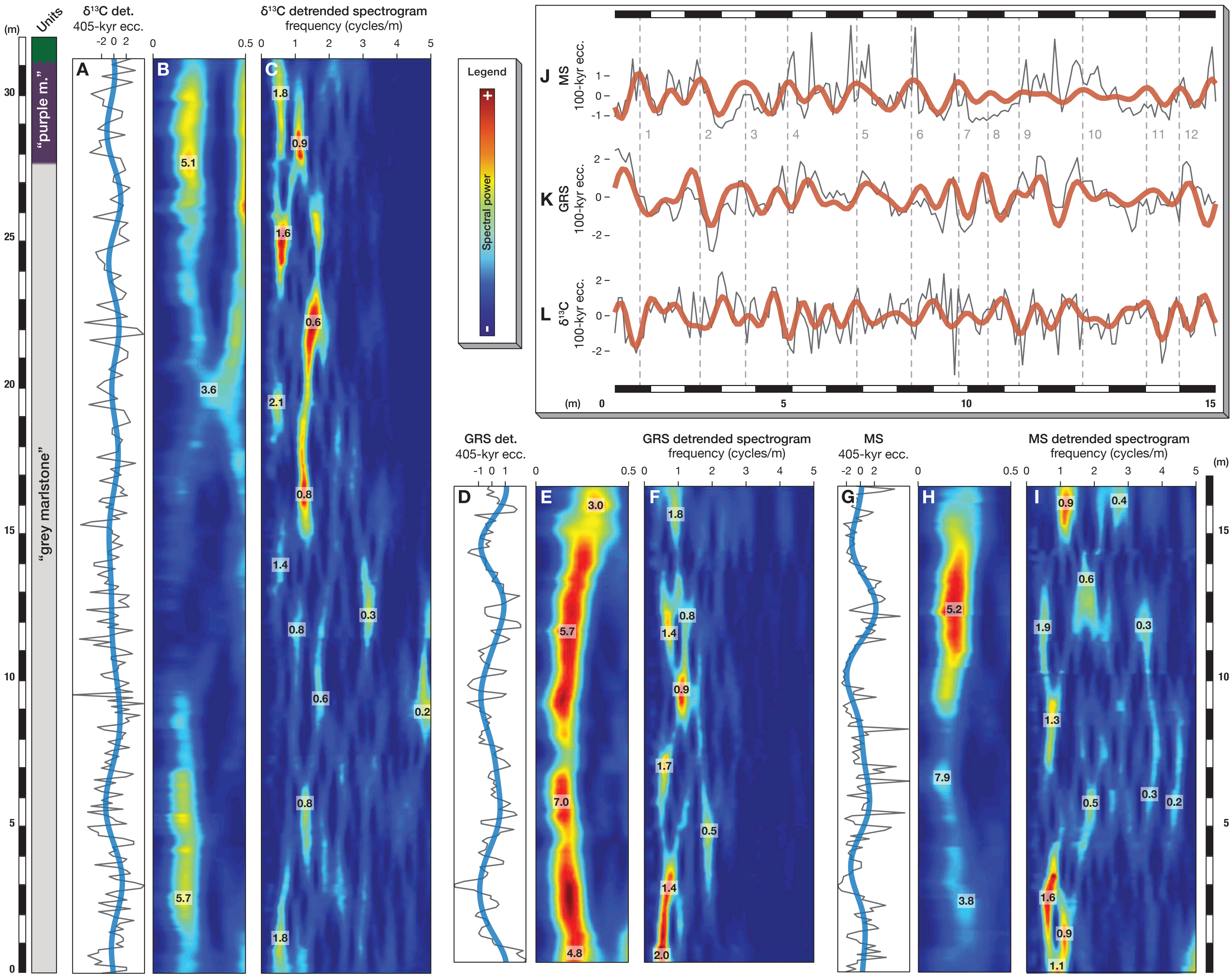

(m)
Units
δ13C det.
405-kyr ecc.
δ13C detrended spectrogram
frequency (cycles/m)
"purple m."
"grey marlstone"
A
B
C
Legend
Spectral power
J
MS
100-kyr ecc.
K
GRS
100-kyr ecc.
L
δ13C
100-kyr ecc.
GRS det.
405-kyr ecc.
GRS detrended spectrogram
frequency (cycles/m)
MS
405-kyr ecc.
MS detrended spectrogram
frequency (cycles/m)
D
E
F
G
H
I

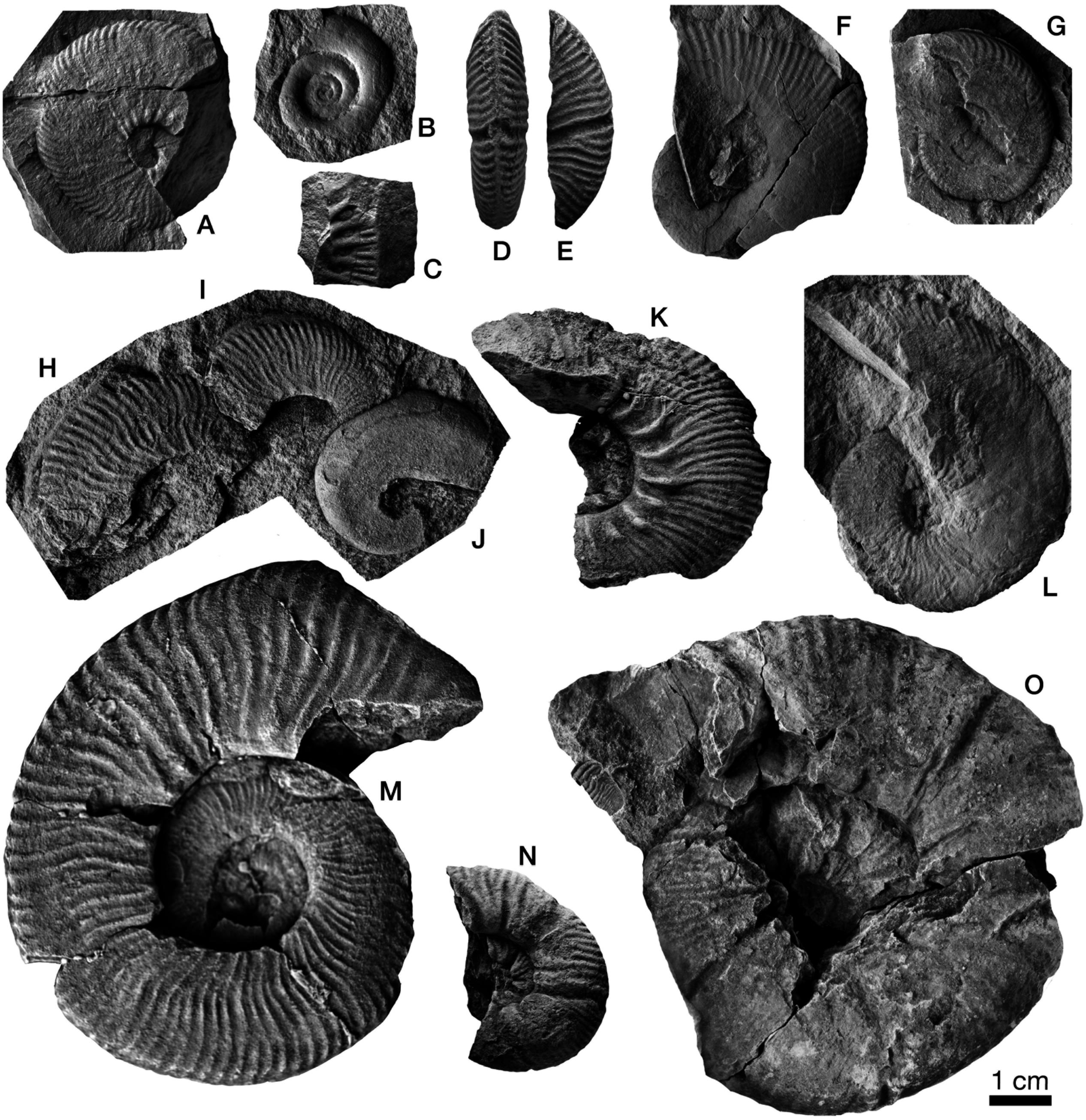
A
B
C
D
E
F
G
H
I
J
K
L
M
N
O
1 cm

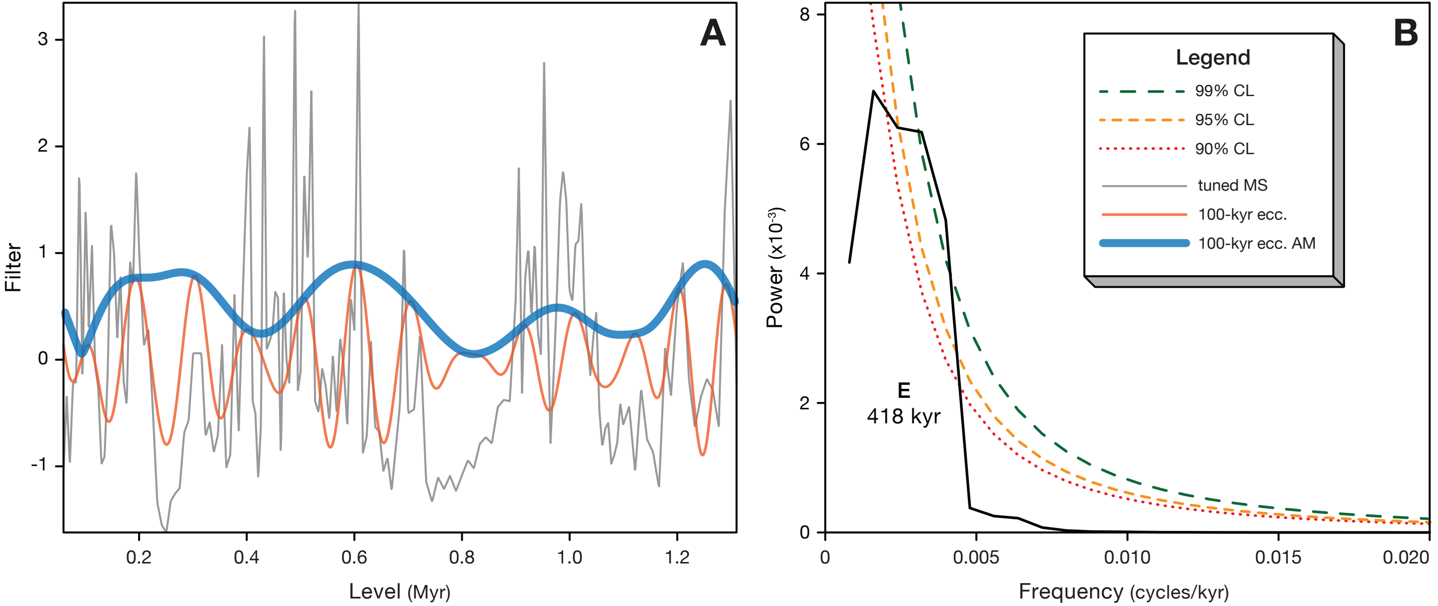
A
Filter
Level (Myr)
3
2
1
0
-1
0.2
0.4
0.6
0.8
1.0
1.2
B
Legend
99% CL
95% CL
90% CL
tuned MS
100-kyr ecc.
100-kyr ecc. AM
E
418 kyr
Power (x10^{-3})
Frequency (cycles/kyr)
8
6
4
2
0
0.005
0.010
0.015
0.020

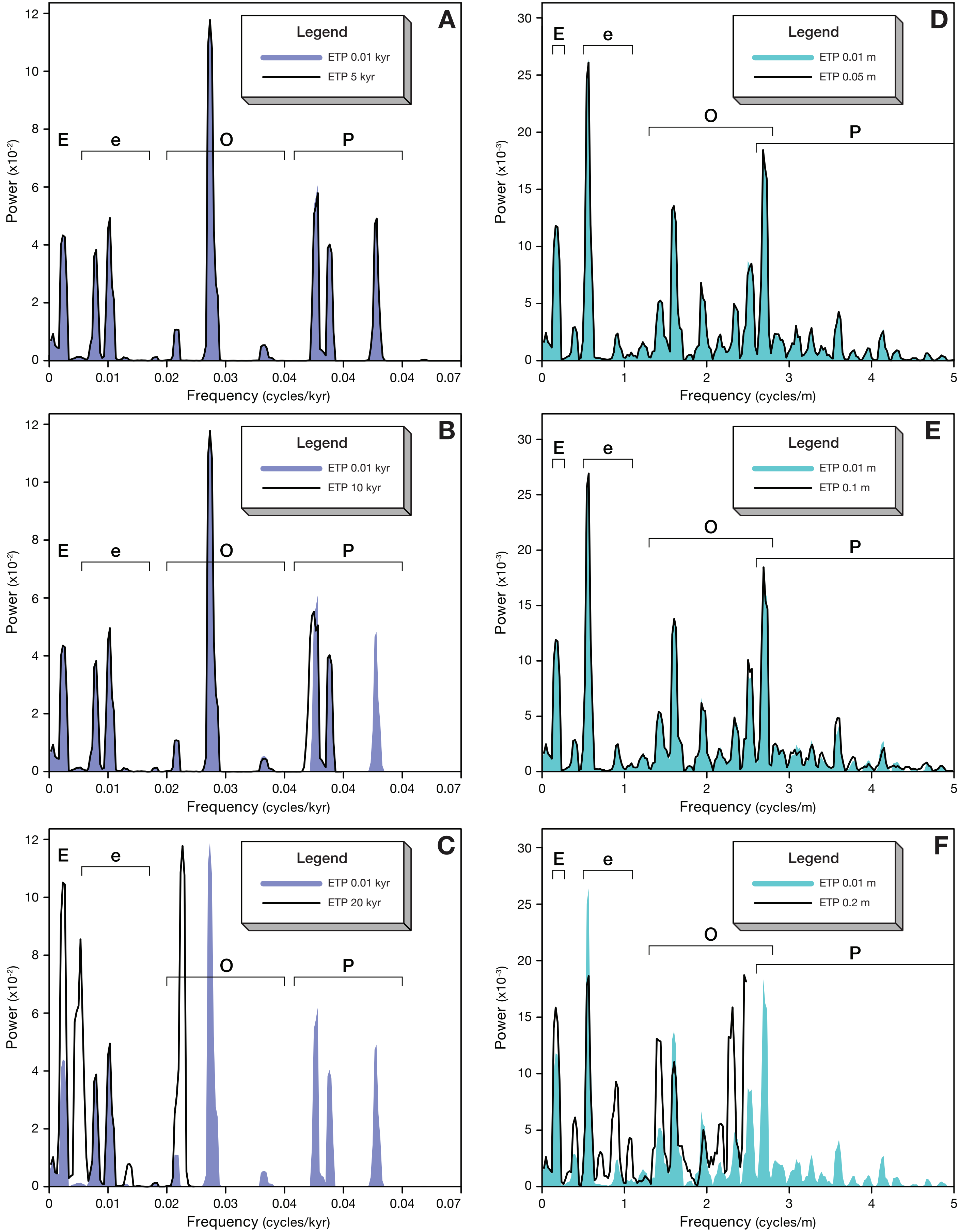
A
Legend
ETP 0.01 kyr
ETP 5 kyr
E
e
O
P
Power (x10⁻²)
Frequency (cycles/kyr)
0
0.01
0.02
0.03
0.04
0.04
0.04
0.07
B
Legend
ETP 0.01 kyr
ETP 10 kyr
C
Legend
ETP 0.01 kyr
ETP 20 kyr
D
Legend
ETP 0.01 m
ETP 0.05 m
Power (x10⁻³)
Frequency (cycles/m)
E
Legend
ETP 0.01 m
ETP 0.1 m
F
Legend
ETP 0.01 m
ETP 0.2 m

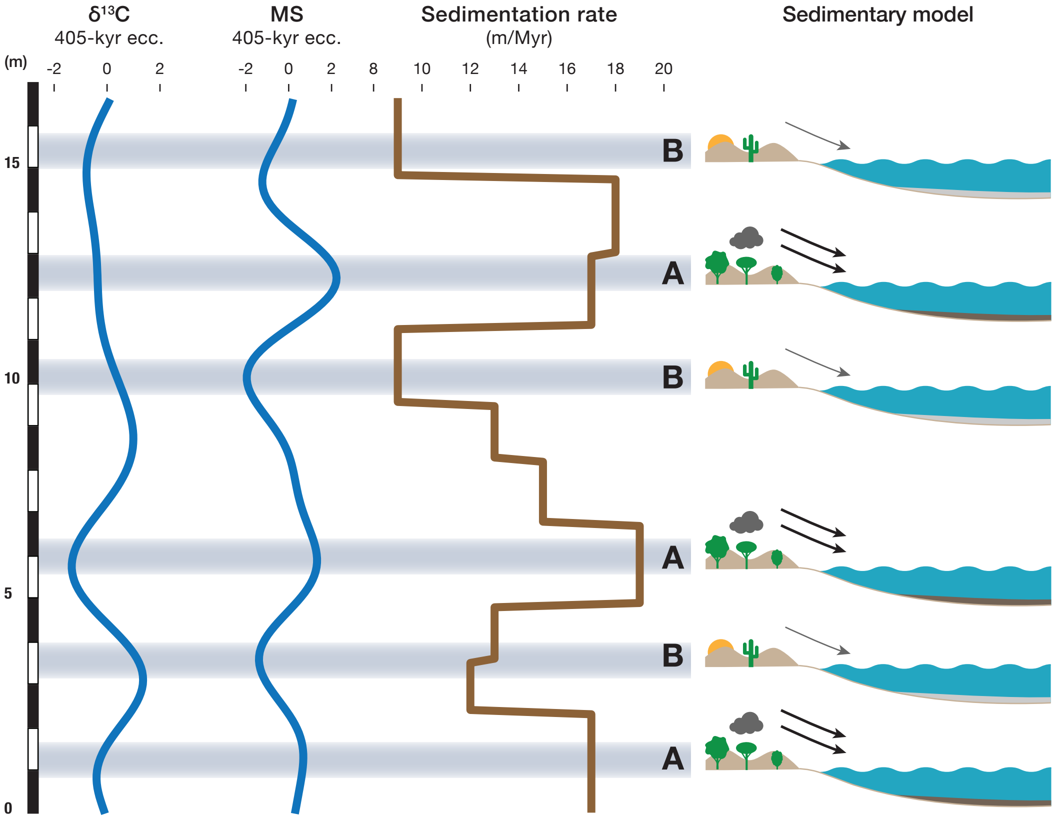

δ13C
405-kyr ecc.
MS
405-kyr ecc.
Sedimentation rate
(m/Myr)
Sedimentary model
(m)
-2
0
2
-2
0
2
8
10
12
14
16
18
20
15
10
5
0
B
A
B
A
B
A

Table 1.

Sample	Level (m)	Unit	$CaCO_3$ (wt%)	Nannoplankton abundance
BQ53	7.3	“grey marlstone”	67	47
BQ54	7.4	“grey marlstone”	62	43
BQ55	7.5	“grey marlstone”	65	45
BQ56	7.6	“grey marlstone”	74	50
BB48	30.2	“purple marlstone”	42	29
BB49	30.4	“purple marlstone”	78	55
BB50	30.6	“purple marlstone”	45	30
BB51	30.8	“purple marlstone”	90	60

Calcium carbonate content (calculated from XRF data) and total nannoplankton abundance (counts of entire specimens in 40 fields of view) of samples collected from the “grey marlstone” and the “purple marlstone” units.

Highlights

- Magnetic susceptibility, gamma ray, $\delta^{13}C$, and $\delta^{18}O$ data from the Bersek Formation.
- A new western Tethyan record of the Late Valanginian Weissert Event is described.
- Spectral analysis reveals presence of Milankovitch periodicities in proxy signals.
- Dilution cycles control the sedimentation and the proxy signals.
- Minimum duration of the $\delta^{13}C$ plateau of the Weissert Event is 1.25 Myr long.

Sample	Level (m)	δ ^{13}C (‰ VPDB)	δ ^{18}O (‰ VPDB)
BQm20	0.00	2.36	-4.11
BQm19	0.10	3.07	-2.48
BQm18	0.20	3.08	-3.02
BQm17	0.30	2.22	-3.27
BQm16	0.40	2.43	-3.76
BQm15	0.50	2.19	-3.75
BQm14	0.60	1.95	-3.75
BQm13	0.70	2.29	-3.46
BQm12	0.80	2.31	-2.91
BQm11	0.90	3.01	-3.06
BQm10	1.00	2.85	-2.90
BQm9	1.10	2.98	-2.33
BQm8	1.20	2.98	-2.78
BQm7	1.30	2.93	-2.57
BQm6	1.40	2.60	-3.41
BQm5	1.50	3.04	-3.03
BQm4	1.60	2.80	-2.80
BQm3	1.70	2.85	-2.19
BQm2	1.80	3.31	-2.19
BQm1	1.90	2.78	-2.47
BQ0	2.00	2.60	-3.10
BQ1	2.10	2.26	-3.65
BQ2	2.20	3.24	-2.16
BQ3	2.30	2.57	-3.63
BQ4	2.40	2.30	-4.60
BQ5	2.50	3.08	-2.81
BQ6	2.60	2.81	-2.50
BQ7	2.70	2.52	-3.30
BQ8	2.80	2.80	-2.38
BQ9	2.90	3.50	-1.90
BQ10	3.00	3.57	-1.98
BQ11	3.10	3.29	-2.55
BQ12	3.20	2.81	-3.05
BQ13	3.30	2.62	-2.81
BQ14	3.40	3.22	-2.55
BQ15	3.50	3.13	-1.43
BQ16	3.60	2.92	-2.50
BQ17	3.70	2.20	-5.60
BQ18	3.80	3.03	-2.74
BQ19	3.90	3.11	-2.94
BQ20	4.00	2.71	-2.77
BQ21	4.10	2.60	-2.70
BQ22	4.20	2.80	-2.90

BQ23	4.30	2.71	-3.21
BQ24	4.40	3.25	-2.63
BQ25	4.50	3.31	-2.52
BQ26	4.60	2.97	-2.71
BQ27	4.70	2.30	-3.06
BQ28	4.80	2.33	-3.63
BQ29	4.90	2.11	-3.85
BQ30	5.00	2.03	-3.53
BQ31	5.10	3.06	-2.29
BQ32	5.20	2.84	-1.94
BQ33	5.30	2.74	-2.21
BQ34	5.40	2.54	-2.74
BQ35	5.50	2.04	-4.30
BQ36	5.60	3.01	-2.34
BQ37	5.70	2.10	-3.90
BQ38	5.80	2.74	-2.90
BQ39	5.90	2.41	-3.17
BQ40	6.00	2.60	-2.37
BQ41	6.10	2.99	-2.58
BQ42	6.20	2.38	-3.32
BQ43	6.30	2.16	-2.89
BQ44	6.40	2.50	-2.98
BQ45	6.50	2.84	-3.07
BQ46	6.60	2.16	-4.39
BQ47	6.70	3.13	-2.52
BQ48	6.80	3.25	-2.07
BQ49	6.90	2.79	-2.47
BQ50	7.00	2.42	-2.76
BQ51	7.10	2.71	-3.60
BQ52	7.20	2.46	-3.25
BQ53	7.30	2.70	-2.90
BQ54	7.40	2.90	-2.92
BQ55	7.50	2.53	-2.79
BQ56	7.60	2.74	-2.46
BQ57	7.70	3.18	-2.16
BQ58	7.80	2.80	-3.30
BQ59	7.90	2.64	-2.57
BQ60	8.00	3.03	-2.64
BQ61	8.10	2.95	-2.53
BQ62	8.20	3.10	-1.99
BQ63	8.30	2.50	-3.00
BQ64	8.40	2.26	-3.78
BQ65	8.50	2.98	-1.97
BQ66	8.60	3.23	-1.89

BQ67	8.70	3.13	−1.94
BQ68	8.80	3.45	−1.80
BQ69	8.90	2.85	−2.73
BQ70	9.00	3.19	−2.05
BQ71	9.10	2.69	−2.23
BQ72	9.20	3.61	−1.79
BQ73	9.30	2.60	−2.96
BQ74	9.40	3.32	−2.50
BQ75	9.50	1.60	−4.70
BQ76	9.60	3.30	−2.45
BQ77	9.70	2.80	−2.40
BQ78	9.80	3.00	−2.45
BQ79	9.90	3.22	−1.96
BQ80	10.00	2.94	−2.23
BQ81	10.10	2.49	−4.17
BQ82	10.20	2.40	−2.90
BQ83	10.30	2.81	−2.92
BQ84	10.40	2.90	−2.50
BQ85	10.50	2.91	−1.28
BQ86	10.60	3.12	−2.23
BQ87	10.70	2.71	−2.82
BQ88	10.80	2.71	−2.65
BQ89	10.90	3.25	−2.11
BQ90	11.00	3.08	−2.33
BQ91	11.10	2.82	−2.27
BQ92	11.20	2.20	−3.10
BQ93	11.30	2.66	−3.02
BQ94	11.40	1.77	−3.20
BQ95	11.50	2.60	−3.60
BQ96	11.60	2.86	−2.29
BQ97	11.70	3.25	−1.94
BQ98	11.80	2.59	−3.10
BQ99	11.90	2.93	−2.52
BQ100	12.00	2.30	−3.20
BQ101	12.10	2.71	−3.07
BQ102	12.20	2.90	−2.50
BQ103	12.30	2.70	−3.10
BQ104	12.40	1.99	−3.04
BQ105	12.50	3.16	−2.05
BQ106	12.60	3.09	−2.17
BQ107	12.70	2.94	−2.19
BQ108	12.80	3.07	−2.63
BQ109	12.90	3.20	−1.88
BQ110	13.00	2.06	−3.30

BQ111	13.10	2.77	-2.36
BQ112	13.20	2.90	-2.20
BQ113	13.30	2.53	-2.79
BQ114	13.40	2.63	-2.86
BQ115	13.50	2.60	-2.80
BQ116	13.60	2.26	-2.76
BQ117	13.70	2.53	-2.58
BQ118	13.80	2.80	-2.41
BQ119	13.90	2.16	-2.81
BQ120	14.00	2.24	-3.52
BQ121	14.10	2.73	-2.66
BQ122	14.20	2.87	-2.07
BQ123	14.30	2.65	-2.61
BQ124	14.40	2.60	-2.41
BQ125	14.50	2.83	-1.85
BQ126	14.60	3.04	-2.15
BQ127	14.70	2.74	-2.19
BQ128	14.80	2.78	-2.69
BQ129	14.90	2.93	-2.19
BQ130	15.00	2.68	-2.58
BQ131	15.10	2.73	-2.28
BQ132	15.20	2.61	-2.41
BQ133	15.30	1.75	-3.75
BQ134	15.40	2.09	-2.74
BQ135	15.50	2.90	-2.20
BQ136	15.60	2.73	-3.17
BQ137	15.70	3.13	-2.17
BQ138	15.80	2.77	-2.46
BQ139	15.90	2.50	-2.80
BQ140	16.00	2.73	-2.83
BQ141	16.10	2.28	-2.95
BQ142	16.20	2.40	-2.80
BQ143	16.30	3.15	-2.04
BQ144	16.40	2.95	-2.01
BQ145	16.50	3.00	-2.20
BQ146	16.60	2.86	-3.38
BQ147	16.70	2.74	-2.58
BQ148	16.80	2.30	-2.50
BC1	17.00	2.86	-2.01
BC2	17.20	2.63	-2.25
BC3	17.40	3.35	-1.71
BC4	17.60	2.19	-3.99
BC5	17.80	2.76	-2.00
BC6	18.00	2.83	-2.02

BC7	18.20	2.91	−1.85
BC8	18.40	2.63	−2.45
BC9	18.60	2.58	−2.40
BC10	18.80	3.10	−1.88
BC11	19.00	2.99	−2.04
BC12	19.20	2.88	−2.12
BC13	19.40	1.91	−3.39
BC14	19.60	2.75	−2.89
BC15	19.80	2.38	−2.48
BC16	20.00	2.11	−2.64
BC17	20.20	2.31	−2.33
BC18	20.40	2.83	−2.01
BC19	20.60	2.35	−2.51
BB1	20.80	2.60	−2.20
BB2	21.00	2.90	−1.70
BB3	21.20	2.90	−2.30
BB4	21.40	2.60	−2.50
BB5	21.60	1.85	−2.79
BB6	21.80	3.30	−1.60
BB7	22.00	3.10	−2.00
BB8	22.20	1.64	−3.39
BB9	22.40	2.85	−1.84
BB10	22.60	2.41	−1.99
BB11	22.80	1.95	−2.60
BB12	23.00	2.59	−2.32
BB13	23.20	2.71	−2.05
BB14	23.40	2.37	−2.66
BB15	23.60	2.22	−2.67
BB16	23.80	2.46	−2.09
BB17	24.00	1.97	−2.67
BB18	24.20	2.00	−3.26
BB19	24.40	1.76	−3.08
BB20	24.60	1.72	−3.56
BB21	24.80	2.18	−2.27
BB22	25.00	2.60	−2.11
BB23	25.20	2.31	−1.90
BB24	25.40	2.30	−2.10
BB25	25.60	2.50	−2.10
BB26	25.80	1.50	−3.20
BB27	26.00	2.20	−2.40
BB28	26.20	2.30	−2.40
BB29	26.40	1.90	−3.00
BB30	26.60	2.20	−2.40
BB31	26.80	2.40	−2.10

BB32	27.00	1.90	-3.50
BB33	27.20	1.90	-2.40
BB34	27.40	2.20	-2.10
BB35	27.60	2.10	-2.20
BB36	27.80	2.00	-2.00
BB37	28.00	1.08	-3.10
BB38	28.20	1.43	-2.72
BB39	28.40	1.28	-4.20
BB40	28.60	2.04	-1.71
BB41	28.80	1.19	-2.64
BB42	29.00	1.37	-2.49
BB43	29.20	1.85	-1.68
BB44	29.40	1.85	-1.76
BB45	29.60	1.20	-3.43
BB46	29.80	1.20	-2.74
BB47	30.00	0.79	-3.84
BB48	30.20	1.26	-2.94
BB49	30.40	1.88	-1.48
BB50	30.60	1.03	-3.09
BB51	30.80	1.91	-1.59
BB52	31.00	1.20	-2.03
BB53	31.20	1.67	-1.30

GRS (ppm)	MS (m^3/kg)	CaCO3 (wt%)	Total nannoplank
	4.025E-07		
	5.254E-07		
	3.631E-07		
46.50	5.009E-07		
46.77	4.804E-07		
45.23	8.902E-07		
44.33	4.379E-07		
46.00	7.695E-07		
42.50	5.186E-07		
38.60	6.682E-07		
38.03	4.202E-07		
37.93	3.657E-07		
35.03	2.080E-07		
34.30	2.147E-07		
34.73	3.765E-07		
35.13	6.633E-07		
36.93	5.951E-07		
36.67	4.286E-07		
35.97	5.479E-07		
33.27	3.394E-07		
33.80	2.895E-07		
35.60	5.739E-07		
38.57	5.258E-07		
39.30	7.573E-07		
38.83	1.685E-06		
37.07	4.121E-07		
37.20	4.478E-07		
34.33	2.923E-07		
32.83	1.131E-07		
27.83	7.355E-08		
27.47	6.266E-08		
30.07	1.287E-07		
34.90	1.481E-07		
35.87	1.633E-07		
36.23	2.767E-07		
34.90	3.062E-07		
34.07	4.423E-07		
40.13	1.595E-06		
40.17	4.520E-07		
38.10	2.949E-07		
34.93	3.272E-07		
33.60	2.733E-07		
35.40	3.126E-07		

35.70	4.936E-07		
35.93	2.572E-07		
34.53	2.874E-07		
35.73	6.085E-07		
38.57	3.358E-07		
39.10	6.150E-07		
42.60	8.586E-07		
38.03	9.556E-07		
34.10	4.170E-07		
33.97	3.944E-07		
39.90	2.678E-07		
43.27	3.829E-07		
42.43	1.170E-06		
38.50	5.288E-07		
40.20	1.703E-06		
41.50	5.653E-07		
39.73	6.468E-07		
37.50	6.354E-07		
36.43	3.181E-07		
37.53	6.560E-07		
36.43	5.149E-07		
37.75	4.691E-07		
36.87	6.317E-07		
37.23	1.250E-06		
35.50	4.523E-07		
35.73	4.885E-07		
36.17	8.726E-07		
38.67	6.956E-07		
41.23	1.040E-06		
40.40	4.219E-07		
39.47	3.976E-07	67	47
37.60	4.814E-07	62	43
36.80	4.420E-07	65	45
37.43	3.713E-07	74	50
39.07	4.968E-07		
37.03	3.795E-07		
32.80	5.227E-07		
34.27	4.634E-07		
32.80	3.397E-07		
33.53	5.876E-07		
33.40	5.181E-07		
35.23	1.171E-06		
34.77	2.676E-07		
35.40	2.973E-07		

34.33	4.774E-07
35.83	3.043E-07
34.73	2.898E-07
32.83	2.073E-07
33.03	2.278E-07
31.33	1.574E-07
29.43	2.363E-07
33.57	3.146E-07
38.37	6.314E-07
39.50	2.871E-07
32.67	2.892E-07
30.27	4.310E-07
29.37	1.366E-07
30.10	9.150E-08
30.83	1.340E-07
33.17	1.061E-07
38.47	1.267E-07
39.40	9.221E-08
34.53	1.178E-07
35.00	1.425E-07
33.50	1.221E-07
32.77	1.659E-07
32.40	1.743E-07
33.43	1.579E-07
31.90	2.252E-07
34.00	2.357E-07
35.30	2.295E-07
38.60	4.255E-07
39.97	6.819E-07
38.30	2.344E-07
35.97	4.601E-07
35.00	5.159E-07
42.67	3.742E-07
42.73	5.264E-07
41.80	3.453E-07
37.43	2.987E-07
33.97	8.815E-07
33.27	4.217E-07
33.33	1.212E-07
33.30	2.574E-07
37.50	4.091E-07
38.97	5.970E-07
40.53	6.587E-07
42.23	5.996E-07

37.57	4.259E-07
37.93	4.043E-07
37.93	5.181E-07
37.93	5.260E-07
34.87	6.062E-07
35.27	3.980E-07
36.10	3.375E-07
36.30	2.719E-07
33.33	3.512E-07
33.33	4.015E-07
32.93	2.126E-07
33.23	1.445E-07
32.77	1.834E-07
30.80	1.985E-07
28.43	1.216E-07
29.27	1.423E-07
33.93	1.703E-07
32.97	2.520E-07
34.17	2.128E-07
31.53	2.524E-07
31.77	1.277E-07
34.83	2.954E-07
33.07	1.985E-07
33.07	1.772E-07
32.80	1.097E-07
35.43	3.863E-07
33.13	2.977E-07
29.87	4.749E-07
40.07	5.631E-07
40.83	3.351E-07
39.83	2.418E-07
35.60	3.027E-07
36.20	3.384E-07
35.70	3.167E-07
32.80	2.433E-07
34.70	6.668E-07
33.00	8.825E-07
33.37	3.087E-07

42	29
78	55
45	30
90	60

ton abundance

(m)
Formation
Informal units
Lithology
Sample number
Ammonites
Lábatlan Sandstone Fm.
"green marker bed"
"purple marlstone"